8-2023

Constraining High Temperature Deformation and Metamorphism in the Southern Wet Mountains, Colorado, USA: Implications for the Regional Extent of the Picuris Orogeny

Sarah Morse
University of Arkansas-Fayetteville

Constraining High Temperature Deformation and Metamorphism in the Southern Wet Mountains, Colorado, USA: Implications for the Regional Extent of the Picuris Orogeny

A thesis submitted in partial fulfillment
of the requirements for the degree of
Master of Science in Geology

by

Sarah Morse
University of Nebraska – Omaha
Bachelor of Science in Geology, 2021

August 2023
University of Arkansas

This thesis is approved for recommendation to the Graduate Council:

_____
Gregory Dumond, Ph.D.
Thesis Director

_____
Adriana Potra, Ph.D.
Committee Member

_____
Barry Shaulis, Ph.D.
Committee Member

_____
Andrew Lamb, Ph.D.
Committee Member

Abstract

The Wet Mountains of Colorado are underlain by exhumed Proterozoic metamorphic rock that lies north of the recently identified 1.46 to 1.40 Ga Picuris orogen in northern New Mexico. The Picuris orogen is inferred to have formed in response to a Mesoproterozoic (ca. 1.49-1.40 Ga) contractional to transpressional event extrapolated to be regional in extent. It has been proposed that the Picuris orogen composes the westernmost tectonic segment of the Pinware-Baraboo-Picuris orogen that formed along an evolving convergent margin that becomes younger from northeast to southwest. This study is focused on the record of high temperature deformation, metamorphism, and plutonism in the southern Wet Mountains interpreted as a consequence of Mesoproterozoic tectonism related to the Picuris orogeny. Geochronology results yielded two populations: ~ 1.45 Ga age of crystallization for granitic intrusions and ~ 1.7 Ga date for a metasedimentary rock. P-T thermobarometric results for a Grt + Sil + Crd + Bt + Kfs + Pl + Qtz migmatite yielded inferred peak conditions of > 0.6 GPa and > 700^{o}C. These results suggest that the Picuris Orogeny was the deformative and metamorphic event that displaced sediments to > 0.6 GPa and caused a regional overprinting of foliation throughout the Wet Mountains.

Table of Contents

Introduction

During the Proterozoic, accretionary rocks were emplaced along a 1,300 km wide orogenic zone that extends from southern Wyoming to northern Mexico (Karlstrom et al., 1987). These accretionary rocks are indicative of continental growth that involved the addition of island-arc terranes to North America, referred to as the continental landmass Laurentia (Karlstrom et al., 2001). In Arizona between the Colorado Plateau and the Basin and Range province, Karlstrom et al. (1987) recognized that Proterozoic plutonic rocks are older to the northwest and younger to the southeast. The Yavapai Province rocks consist predominantly of juvenile arc terranes that were accreted to the Laurentian margin 1.78 to 1.70 Ga along a belt from Colorado to Arizona and New Mexico (Fig. 1B; Jones et al., 2010). The Mazatzal Province lies south of the Yavapai Province and was accreted to southern Laurentia during the Mazatzal orogeny ca. 1.66 to 1.60 Ga (Silver, 1965; Karlstrom and Bowring, 1988; Amato et al., 2008).

Following these accretionary events, an ~150 m.y. tectonic lull occurred prior to renewed southward growth of Laurentia during the Mesoproterozoic (Jones et al., 2010). This renewal is indicated through widespread granitic magmatism and regional high-temperature, low-pressure metamorphism from 1.47 to 1.36 Ga. Circa 1.4 Ga magmatism was previously thought to be anorogenic (Bickford et al., 1989), however recent studies consider plutonism to have occurred contemporaneous with contractional or transpressional plate-margin tectonism (Nyman et al., 1994). Daniel et al. (2022) correlated the Pinware, Baraboo, and Picuris orogens and suggested they represent a ~5,000 km-long orogen that developed progressively along its strike-length, i.e., with tectonism and magmatism occurring at different times at ca. 1.52-1.34 Ga (Fig. 1A). The Picuris orogen represents the southwestern end of this trans-Laurentian orogen and experienced

the youngest episodes of magmatism and metamorphism (Jones et al., 2010; Daniel et al., 2013, 2022).

Studies conducted in northern New Mexico, specifically in the Picuris Mountains (Fig. 1B), investigated detrital zircon geochronology of the Trampas Group and Marqueñas Formation (Jones et al., 2011; Doe et al., 2012, 2013; Daniel et al., 2013). These studies concluded that the presumed Paleoproterozoic metamorphic rocks have Mesoproterozoic protolith ages, with depositional ages for the aforementioned units occurring ca. 1.49 to 1.46 Ga (Daniel et al., 2013). These results suggested the rocks experienced one amphibolite-facies regional metamorphic and contractional to transpressional deformation event, termed the Picuris orogeny (Daniel et al., 2013). Further supporting these results are studies conducted by Aronoff et al. (2016) and Holland et al. (2020), which concluded that the Precambrian tectonic history of northern New Mexico was the result of a single progressive Mesoproterozoic tectonic event. However, Mesoproterozoic sedimentary rocks in the Picuris Mountains and adjacent ranges in northern New Mexico were deposited unconformably on the Paleoproterozoic Vadito Group, which may have been deposited during active tectonism related to the Yavapai Orogen (Daniel et al., 2013).

This study focused on the record of high temperature deformation, metamorphism, and plutonism in the southern Wet Mountains interpreted as a consequence of Mesoproterozoic tectonism related to the Picuris orogeny (Jones et al., 2010). Evidence for three deformation events which occurred during the Paleoproterozoic and Mesoproterozoic exists within the Wet Mountains, however timing and impact of these events can be further constrained. The southern Wet Mountains are suggested to have undergone deformation and metamorphism deeper within the crust than other exposed areas in the Wet Mountains. This study utilizes field data, microstructural analysis of thin sections, zircon geochronology, and sample thermobarometry to

determine the pressure and temperature conditions of the southern Wet Mountains to infer rock depth during deformation and metamorphism.

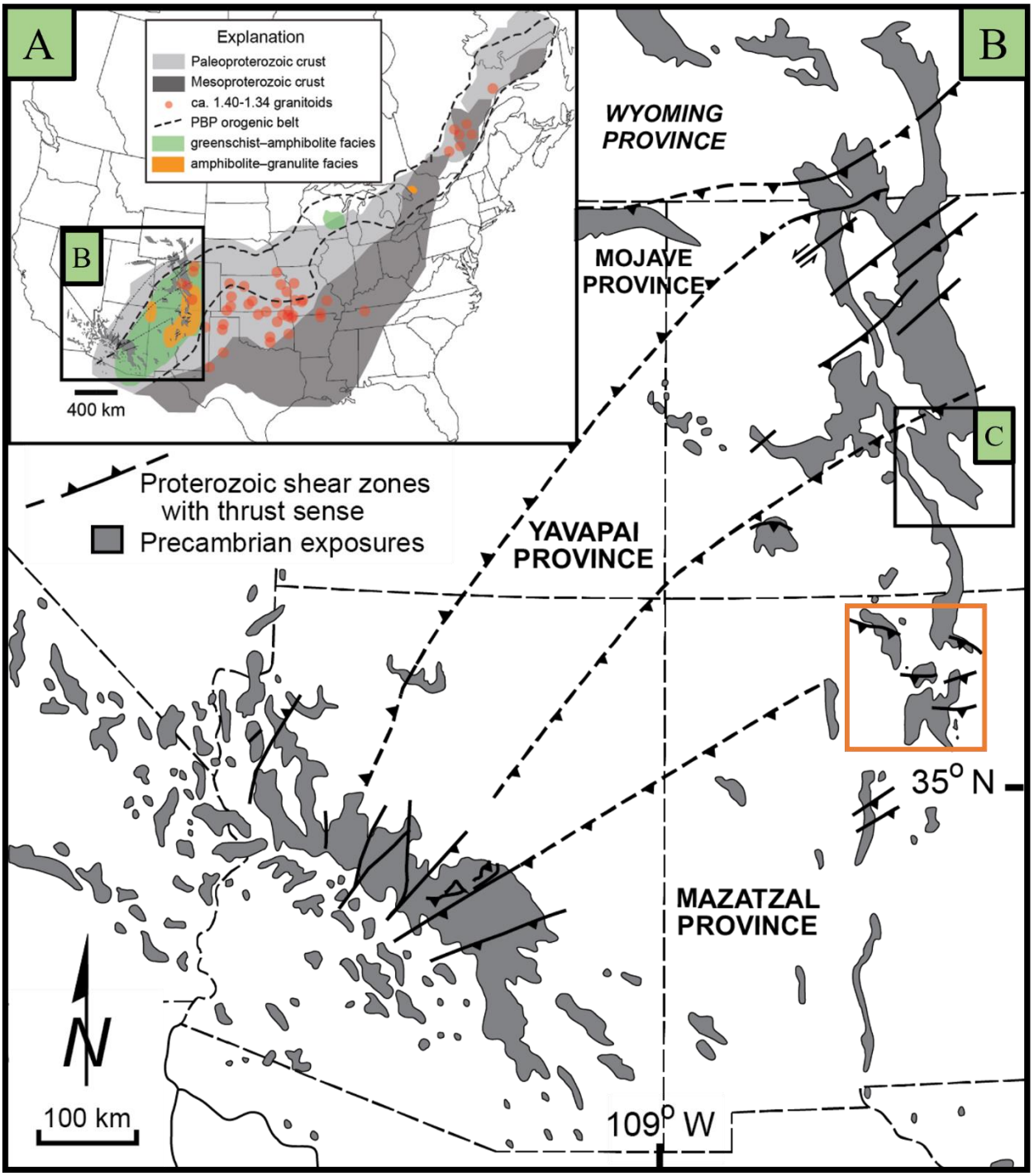

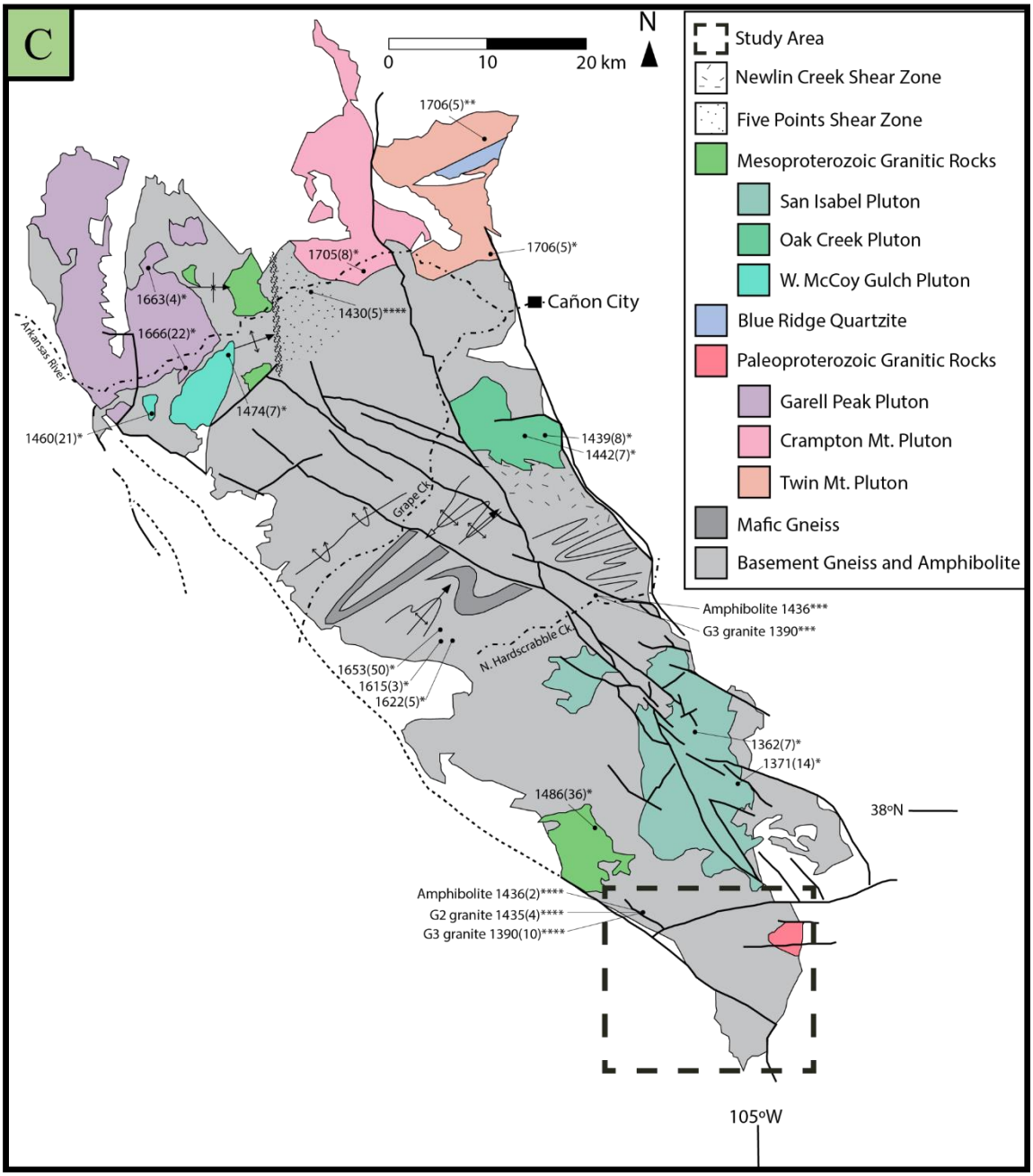

Figure 1: [A] Proterozoic geology outlining crustal age segments, relevant granitic intrusions, and metamorphic facies from Daniel et al. (2022). Proposed Pinware-Baraboo-Picuris orogenic belt outlined. [B] Map of the southwestern United States with exposed Proterozoic provinces and shear zones (modified after Karlstrom et al. 2006). Orange box denotes the study area for Aronoff et al. (2016), including the Picuris Mountains. [C] Proterozoic geologic map for the Wet Mountains, Colorado. Study area noted by the black dashed box. Map based on Tweto (1979), Bickford et al. (1989), Siddoway et al. (2000), and Jones et al. (2010). U-Pb geochronology of Bickford et al. (1989)*, Jones et al. (2009)**, Jones (2005)***, Jones (2010)****.

Geologic Setting

The Wet Mountains of Colorado are underlain by exhumed Proterozoic metamorphic rock that occurs north of the 1.46 - 1.40 Ga Picuris orogen in northern New Mexico (Daniel et al., 2013; Aronoff et al., 2016). The study area in the southern Wet Mountains is dominated by quartzose and quartzofeldspathic gneiss, amphibolite gneiss, and metagabbro (Fig. 2; Boyer, 1962; Jones et al., 2010). These rocks experienced upper-amphibolite to granulite facies metamorphism and multiple episodes of penetrative, coaxial deformation attributed to NW-SE sub-horizontal contraction (Siddoway et al., 2000; Jones et al., 2010; Levine et al., 2013).

Bickford et al. (1989) identified four distinct episodes of igneous activity as recorded by plutons emplaced throughout the Wet Mountains during the Proterozoic. The Mesoproterozoic igneous activity relevant to this study intruded the crust from 1.47 to 1.43 Ga and 1.37 to 1.35 Ga. Intrusive rocks in the Wet Mountains related to these events include the foliated Oak Creek pluton (1436 ± 8 Ma; Bickford et al., 1989) and the undeformed San Isabel pluton (1371-1362 Ma; Bickford et al., 1989). Granite and migmatitic host gneiss exposures in the southern Wet Mountains display evidence for an originally deep crustal position, with a top-to-the-south-southeast transport sense associated with episodes of pervasive lower-crustal flow (Jones, et al., 2010). They recognized that the earliest episode occurred after the emplacement of G_2 granites (e.g. Oak Creek Pluton) and continued through 1.39 Ga.

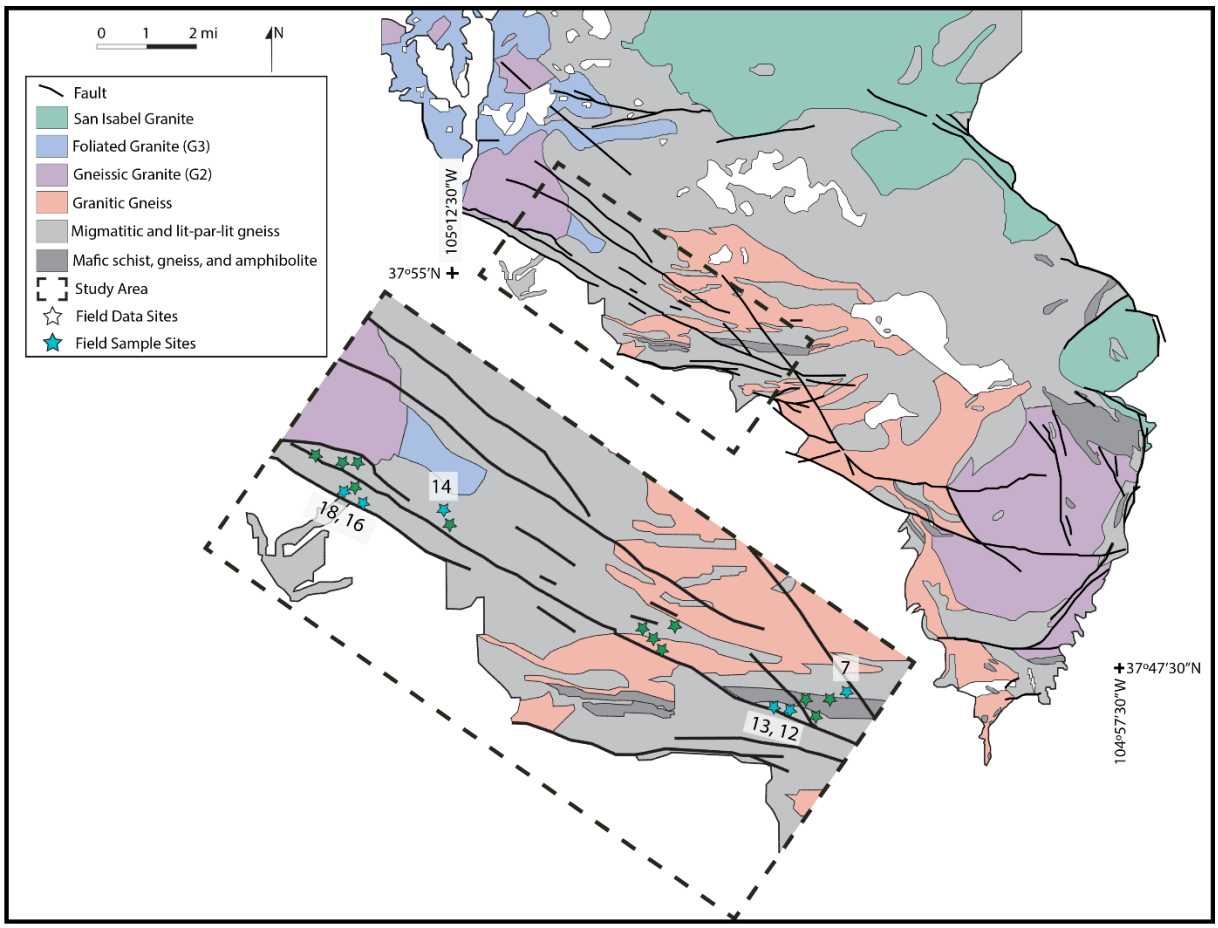

Figure 2: Proterozoic geologic map for the southern Wet Mountains, Colorado. Study area noted by the black dashed box. Field data collected at sites denoted with a star and oriented sample collected from sites with a blue star and labeled. Map based on Boyer (1962) and Jones et al. (2010).

The first deformation event (D_1) recorded in the Wet Mountains is evident in the Texas Creek Domain and Arkansas River Gorge in the northern portion of the range and is interpreted as synchronous with the emplacement of the 1663 ± 4 Ma Garell Peak Pluton (Siddoway et al., 2000; Jones et al., 2010). The second deformation event (D_2) recorded in the Wet Mountains is interpreted as being coeval with the 1474 ± 7 Ma W. McCoy Gulch Pluton during the Mesoproterozoic (Siddoway et al., 2000; Jones et al., 2010). The 1442 ± 7 Ma Oak Creek Pluton is interpreted as being syntectonic with the third deformation event (D_3; Jones et al., 2010).

Overall, evidence for the third deformation event is pervasive throughout the central and southern portions of the Wet Mountains as a result of overprinting and dynamic recrystallization.

Recent studies have worked to constrain the deep-crustal deformation and metamorphism exposed in the Wet Mountains as well as the Front Range of Colorado. In the Front Range, rocks experienced up to amphibolite facies metamorphism during the Paleoproterozoic and the Mesoproterozoic at mid-crustal pressures of ~0.4 GPa and temperatures between 500 – 700^{o}C (Mahatma et al., 2022). South of the Front Range in the northern Wet Mountains, pressure and temperature estimates were constrained for a flecked gneiss that yielded peak metamorphic conditions of 600 – 700^{o}C and pressures between 0.3 – 0.5 GPa (Trumbull, 1988). Host rock exposed north of the Oak Creek Pluton in the central Wet Mountains experienced anatexis and peak metamorphic conditions at ~ 0.7 GPa and ~750^{o} C (Hernández-Montenegro et al., 2019). In the southernmost range, Cullers et al. (1992) worked to constrain the pressure and temperature conditions during emplacement of the San Isabel batholith and determined pressures between 0.5 – 0.7 GPa, equivalent to emplacement depths between 17 – 23 km, assuming an average density for continental crust (~ 2.8 g/cm^{3}).

From north to south along a transect of the Wet Mountains, the presence of migmatites increases as a function of metamorphic grade. This change is indicative of shallow mid-crustal levels in the north with increasing depth towards the south (Jones et al., 2010; Levine et al., 2013). While previous studies have worked to constrain the pressures and temperatures experienced in the Front Range and northern to central Wet Mountains, these conditions have not been assessed for the southern Wet Mountains.

Methodology

Research for this project will address two major questions: 1) the pressure and temperature conditions of the southern Wet Mountains, and 2) the timing and conditions of Mesoproterozoic deformation events. In order to properly address these questions, methods include field work, microscopy, whole rock analysis with an electron microprobe, whole rock composition modeling using Perple_X software, and laser ablation ICP-MS.

Foliation and lineation data were collected at 18 sites (Fig. 2) throughout the southwest portion of the Wet Mountains and cross-analyzed with data collected by Jones et al. (2010). Data were projected onto a geologic map modeled after Jones et al. (2010) and Boyer (1962). 12 thin sections were made from 6 oriented samples collected in the field, spanning 8 km. These samples were cut perpendicular to foliation and parallel to lineation to be made into thin sections to evaluate evidence for sense of shear. Thin section microscopy was utilized for all sections to assess deformative structures as well as petrologic relationships. Zircon grains were noted in 5 thin sections from sites S22-07, S22-14, S22-16, and S22-18 (Fig. 2), and were dated using laser ablation ICP-MS geochronology.

Bulk rock geochemical analysis of major and trace elements was carried out commercially via ICP-MS techniques at Activation Laboratories, Ltd. in Ancaster, Ontario, Canada. This analysis was conducted for site S22-13, a Grt + Sil + Crd + Bt + Kfs + Pl + Qtz metapelite migmatite. Perple_X modeling software was used to construct phase diagrams for the S22-13 bulk composition to constrain the temperature and pressure conditions under which the sample was stable as well as to deduce the potential reactions and processes throughout deformation and metamorphism (Connolly, 1995; Connolly et al., 2002; White et al., 2000, 2014). Solution models used for garnet, biotite, cordierite, mica, and orthopyroxene are from

White et al. (2014), the feldspar solution model is from White et al. (2000), and the ilmenite solution model is from Holland and Powell (2003).

High-spatial resolution X-ray mapping was utilized to identify monazite grains in the polished thin sections. Samples were sent to the University of Massachusetts-Amherst Electron Microprobe/SEM Facility in order to obtain full section X-ray stage maps using the Cameca SX50 and SX100 electron microprobes. Methodologies for monazite analysis were modeled after Williams et al. (2017) and Dumond et al. (2022). Both thin sections from S22-13 and one thin section from S22-14 were sent to the facility for mapping.

Results

Field Data

Foliation data were collected along 4 hiking trails in the southern Wet Mountains (Fig. 3): Cisneros Trail (S22-07 – S22-13), Pole Creek Trail (S22-14 – S22-15), Mountain Park Trail (S22-16 – S22-21), and the Salt Road (S22-22 – S22-25). Table 1 includes recorded foliation data and coordinates for the sites. The strike of foliation is oriented between 220 – 290 and tends to be steeply dipping toward the east and more moderately to the west. There is also a foliation trend from WNW orientation to WSW/SW orientation from east to west in our study area. Foliation data collected by Boyer (1962) was combined with our data into stereonet plots shown in Figure 3. Average strike and dip of foliation for 242 data points is 256, 68^{o}.

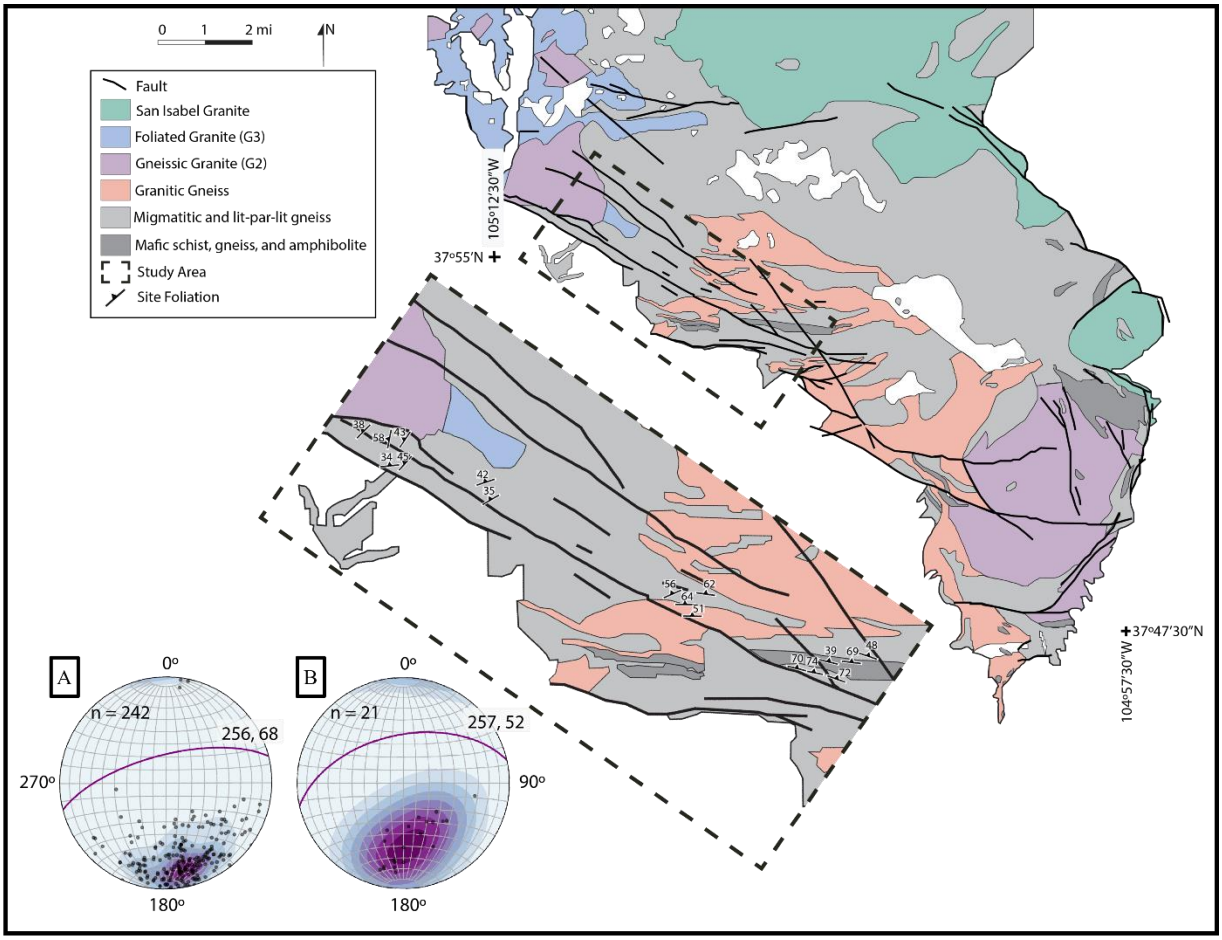

Figure 3: Proterozoic geologic map for the southern Wet Mountains, Colorado. Study area noted by the black dashed box. Site foliation recorded on the study area map. Stereonet plots reflect our data collected in the field as well as data collected by Boyer (1962), [A] Our data + Boyer; [B] Our data. Map based on Boyer (1962) and Jones et al. (2010).

Sample	Coordinates					Foliation		Lineation		Oriented Sample	
ID	Latitude	Longitude	Township	Range	Section	Strike	Dip	Trend	Plunge	Strike	Dip
S22-07	N37.89587	W105.09121	25S	69W	10	288	48			270	54
S22-08	N37.89504	W105.09438	25S	69W	10	276	69				
S22-09	N37.89331	W105.09583	25S	69W	10	289	39				
S22-10	N37.89452	W105.09767	25S	69W	10	283	72				
S22-11			25S	69W	10	276	64				
S22-12	N37.89440	W105.10186	25S	69W	10	275	74			144	45
S22-12	N37.89440	W105.10186	25S	69W	10	285	74				
S22-13	N37.89451	W105.10333	25S	69W	10	283	70			95	23
S22-14	N37.91930	W105.15948	24S	69W	31	251	42	355	50	79	76
S22-14	N37.91930	W105.15948	24S	69W	31	246	29				
S22-15	N37.91865	W105.15823	24S	69W	31	239	35	350	31		
S22-16	N37.92105	W105.17433	24S	70W	36	221	45	349	34	228	40
S22-17	N37.92155	W.105.17487	24S	70W	36	221	34	324	34		
S22-18	N37.92138	W105.17506	24S	70W	36	263	34			207	70
S22-19	N37.92673	W105.17967	24S	70W	25	224	43	350	41		
S22-20	N37.92721	W105.17670	24S	70W	25	190	58				
S22-21	N37.92807	W105.17619	24S	70W	25	233	38				
S22-22	N37.90159	W105.12066	25S	69W	4	270	51	355	50		
S22-23	N37.90249	W105.12093	25S	69W	4	270	64				
S22-24	N37.90320	W105.12165	25S	69W	4	245	56				
S22-25	N37.90470	W105.11904	25S	69W	4	277	62				

Table 1: Data collected at each site in the field with coordinate locations, foliation, lineation, and oriented samples.

S22-14 was a focus site for this study due to its proximity to an outcrop studied by Jones et al. (2010). The outcrop is a Ttn + Ep + Mag + Bt + Kfs + Pl + Qtz granodiorite gneiss interlayered with isoclinal recumbent folds of amphibolite (Fig. 4). Foliations dip northwest with nearly down-dip stretching lineation. Recrystallized feldspar σ-clasts viewed on a surface nearly parallel to lineation and perpendicular to foliation indicate top-to-the-North (normal) shear sense.

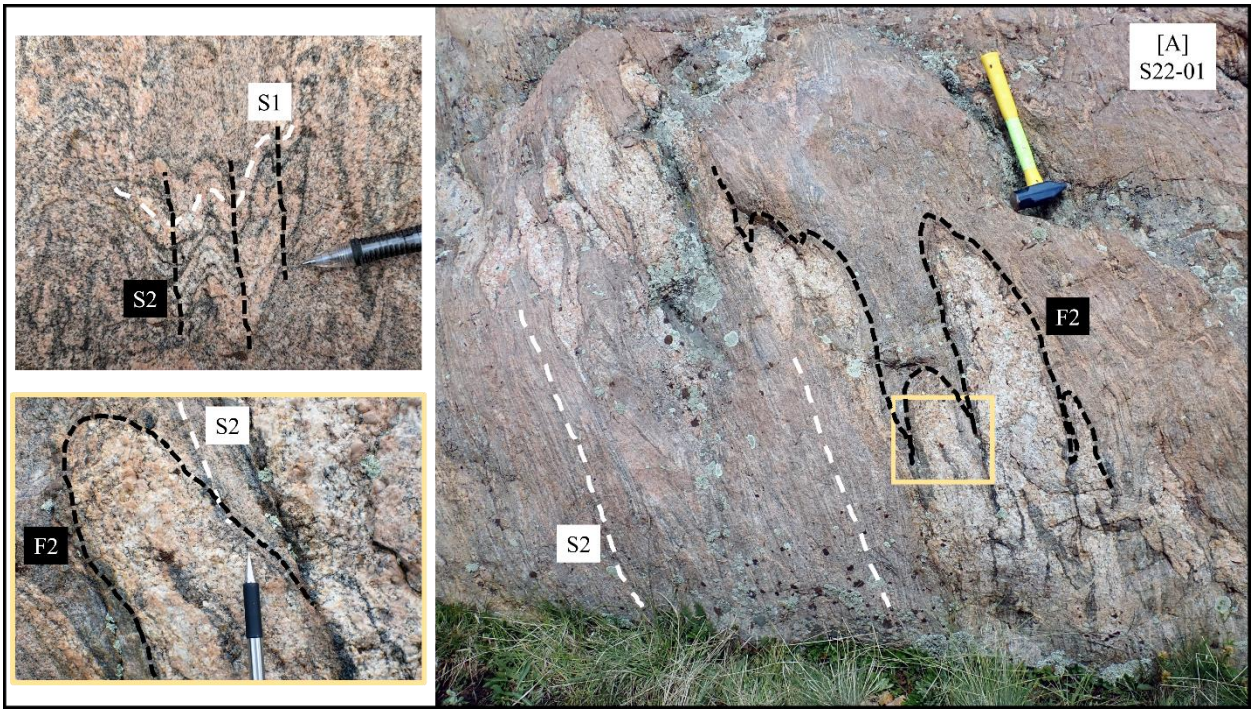

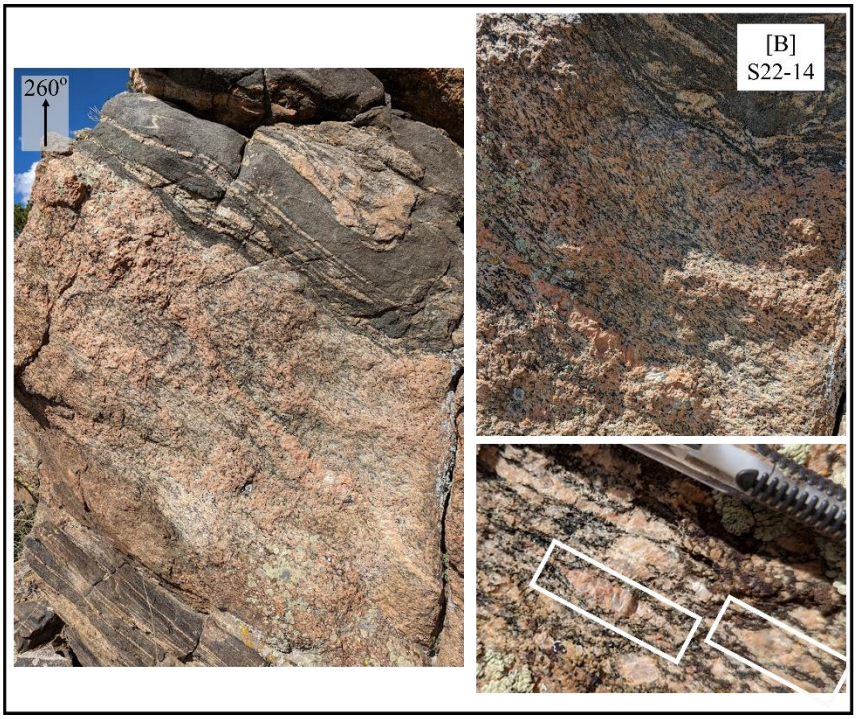

Figure 4: Field photographs depicting structural data. [A] Folded dikes within a migmatite at S22-01. S1 foliation is truncated by the folded granitic dike. The dike is likely pre- or syn-S2/F2. No evidence the dikes experienced the gneissic deformation. [B] Site S22-014, camera view facing 260°. Fabrics dip NW with nearly down-dip stretching lineation. Isoclinally folded amphibolite is interlayered with lit-par-lit gneiss. Recrystallized feldspar σ-clasts viewed on a surface nearly parallel to lineation and perpendicular to foliation indicate top-to-the-North (normal) shear sense.

Microstructural Analysis

S22-07

Sample S22-07 is dominantly K-feldspar and plagioclase with quartz, minor biotite and accessory zircon. Quartz appears as seriate, amoeboid grain boundaries with small grains within or between the larger feldspar grains. Extensive quartz ribbons are also present with deformation banding and chessboard extinction. Feldspar appears to have undergone grain boundary migration recrystallization with lobate boundaries (Fig. 5). Throughout plagioclase grains there is penetrative sericitization and myrmekite along grain boundaries. Sample S22-07 displays well-developed sericite compared to the other sections with distinct aggregates and visible sheets.

S22-12

Quartz is more prevalent in Sample S22-12 compared to the other samples examined, along with biotite, minor K-feldspar and plagioclase. Zircon is present within biotite but is less than 20 μm in length. Grains are more fine, equigranular, and lobate. Feldspar displays deformation twinning and inclusions. Some plagioclase grains appear to display resorbtion along quartz boundaries. Other grains possess inclusions of rectangular plagioclase parallel to cleavage which may represent dislocations (Fig. 5). Biotite is a distinct phase in this section and reflects the dominant foliation for the section. This distinct foliation is likely inherited from the sedimentary origin prior to metamorphism of the region.

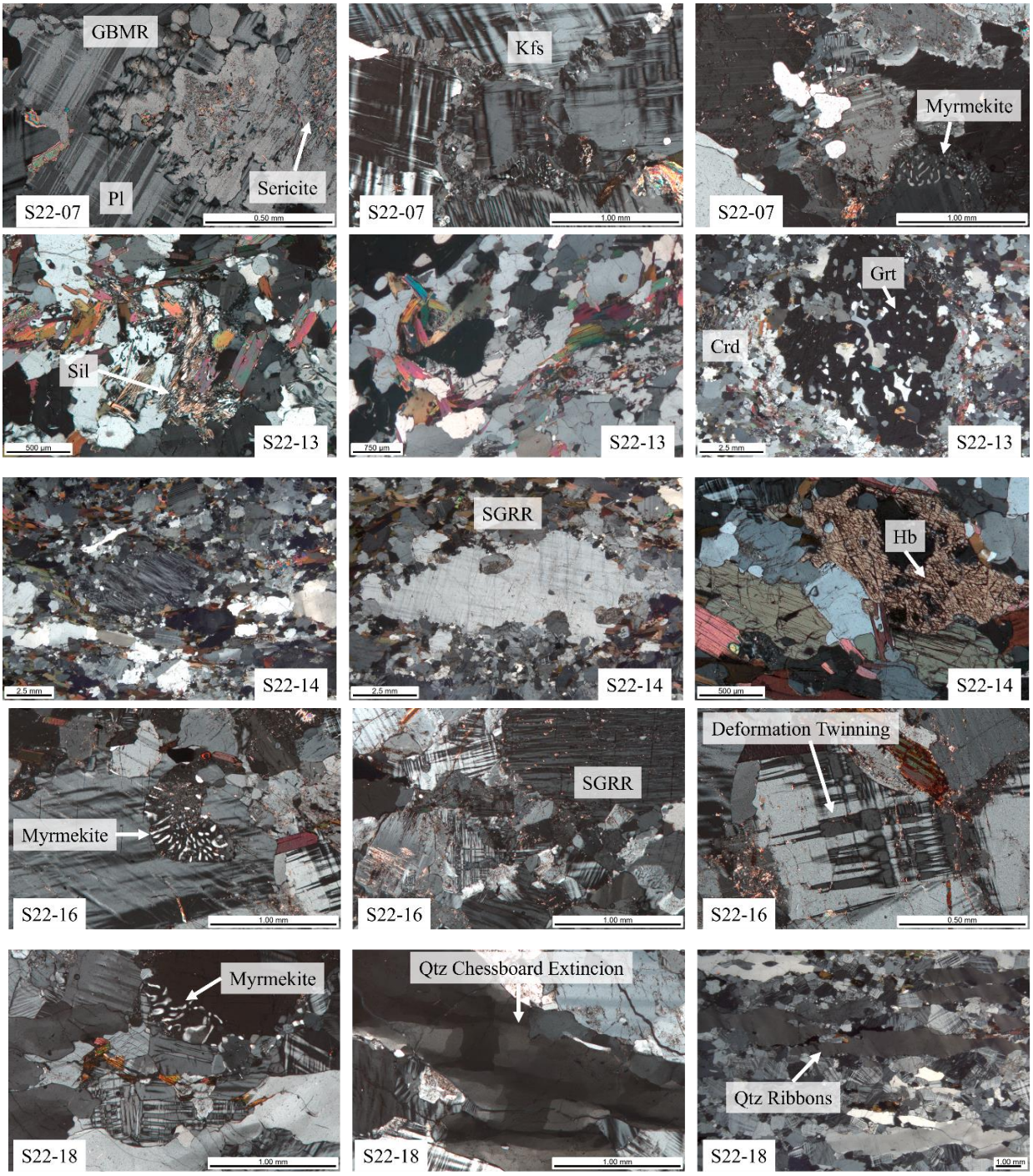

Figure 5: Photomicrographs depicting structural and petrographic relationships within the samples. Evidence for Grain Boundary Migration Recrystallization (GBMR) and Subgrain Rotation Recrystallization (SGRR) pictured. Mineral abbreviations: plagioclase (Pl), K-feldspar (Kfs), quartz (Qtz), biotite (Bt), zircon (Zr), sillimanite (Sil), garnet (Grt), cordierite (Crd), hornblende (Hb).

S22-13

Sample S22-13 is a Grt + Sil + Crd + Bt + Kfs + Pl + Qtz metapelite migmatite with accessory zircon, monazite, and xenotime. Garnet boundaries are anhedral with biotite inclusions and biotite and cordierite along grain boundaries (Fig. 5). The biotite displays alteration haloes and inclusions of zircon and monazite. Cordierite displays polysynthetic twinning and pinite is also present. Cordierite is also a symplectite with quartz grains. Sillimanite appears as clustered, acicular grains throughout the samples. Quartz appears as interlobate grains with undulose and chessboard extinction with deformation bands. Quartz and feldspar display grain boundary migration recrystallization. Similar to Sample S22-12, quartz is a dominant phase within the matrix as opposed to feldspar which is more dominant in the other sections. In contrast to all other samples, Sample S22-13 displays evidence for in-situ partial melting that promotes migmatitic structures.

S22-14

Sample S22-14 is one of the key sections for this study and is a Ttn + Ep + Mag + Bt + Kfs + Pl + Qtz granodiorite lit-par-lit gneiss. Magmatic, euhedral hornblende and magmatic epidote are evident throughout the sample alongside biotite, titanite, sphene, and magnetite with accessory zircon. The matrix overall displays seriate, interlobate grain boundaries. Quartz can be found throughout the sample as ribbons with undulose extinction and chessboard extinction. Feldspars display subgrain rotation recrystallization with well-developed sericite and myrmekite. While in field kinematics were strong or this sample, the thin sections for S22-14 did not display a strong sense of kinematics.

S22-16 and S22-18

Samples S22-16 and S22-18 have quartz ribbons that are the most distinctly developed of all the thin sections and are oriented parallel to foliation with deformation bands and chessboard extinction (Fig. 5). Biotite is evident in both samples but is still a minor phase overall. For Sample S22-16, feldspar grain boundaries are inequigranular and lobate with deformation twinning. Potassium feldspar is dominant in this sample and feldspars display subgrain rotation recrystallization. Plagioclase feldspar displays extensive sericitization with well-developed myrmekite. For sample S22-18, feldspar grain boundaries are seriate lobate and display a distinct core and mantle structure. Sericite and myrmekite are still present, however sericitization is less prevalent overall when compared to other sections. Shear sense indicators for samples S22-16 and S22-18 suggest normal kinematics displayed along relict clasts, quartz ribbons, and biotite foliation, however all indicators are weak and poorly developed throughout the sections.

LA-ICP-MS Geochronology

Zircon LA-ICP-MS geochronology results are displayed in Figure 6. Approximate dates were collected for 5 thin sections across 4 sites (Samples S22-07, S22-14, S22-16, S22-18).

S22-07

Sample S22-07-2 is the southeastern most site in our study area and zircon mineralization is concentrated along the foliation planes defined by biotite. Zircon grains are dominantly concentrated along biotite grain boundaries as opposed to within biotite. Zircon grains for site S22-07 are the largest of all the sites with maximum lengths > 300 μm, however zircon is overall less abundant. This site yielded an average date of 1717 ± 36 Ma and dates derived from this

sample possess a large MSWD compared to the other younger samples. Dates for this sample ranged from 1677 Ma to 1773 Ma. Sample S22-07 as a whole is a lit-par-lit gneiss with granitic injections and we believe that the dates derived from sample S22-07-2 possess a large MSWD due to mixed dates between the granitic injections and Paleoproterozoic metasediments. These older dates for sample S22-07 are consistent with dates reported by Bickford et al. (1989) for foliated plutons in the Mt. Tyndall area, the Garell Peak pluton, and Phantom Canyon pluton.

S22-14-1

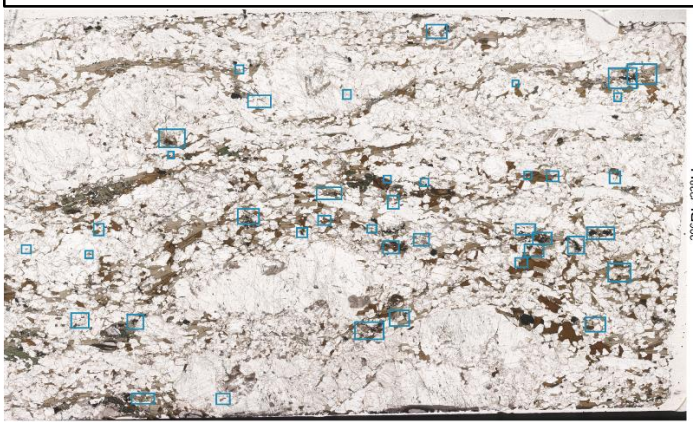

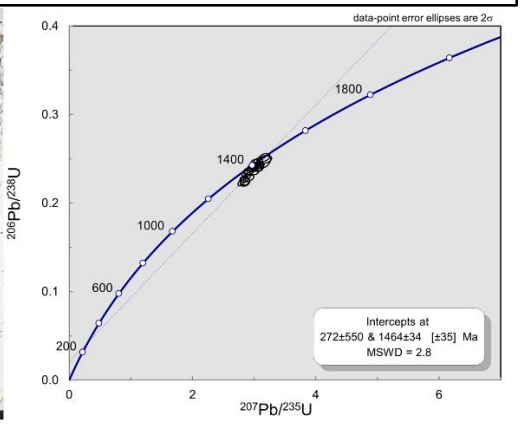

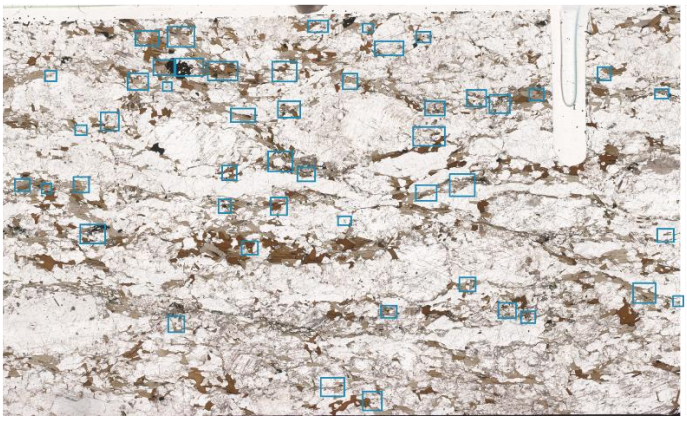

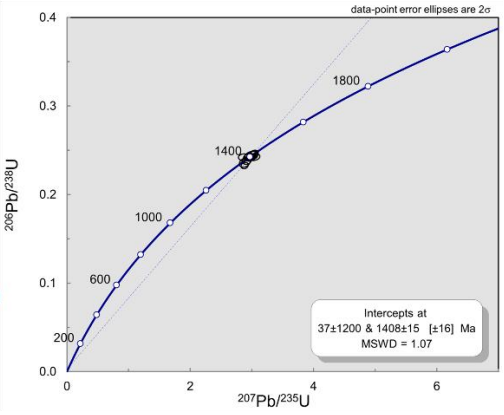

S22-16

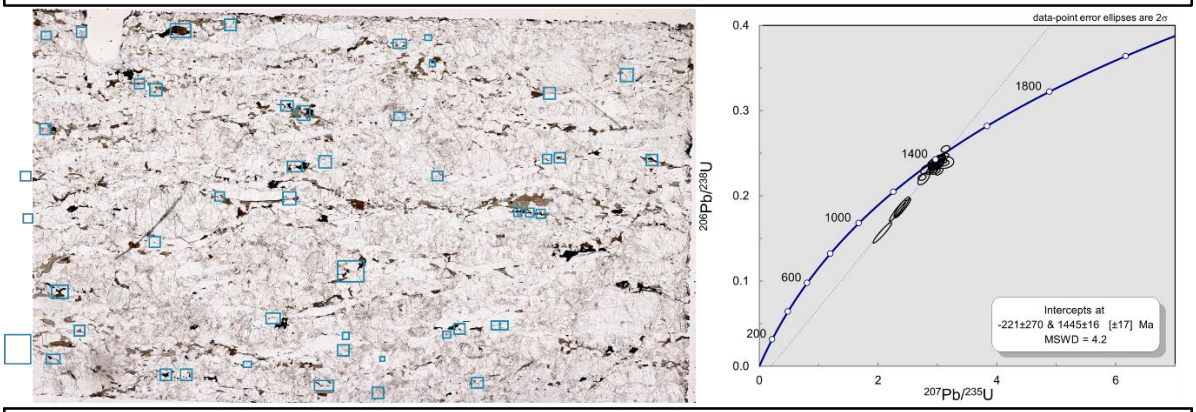

S22-18

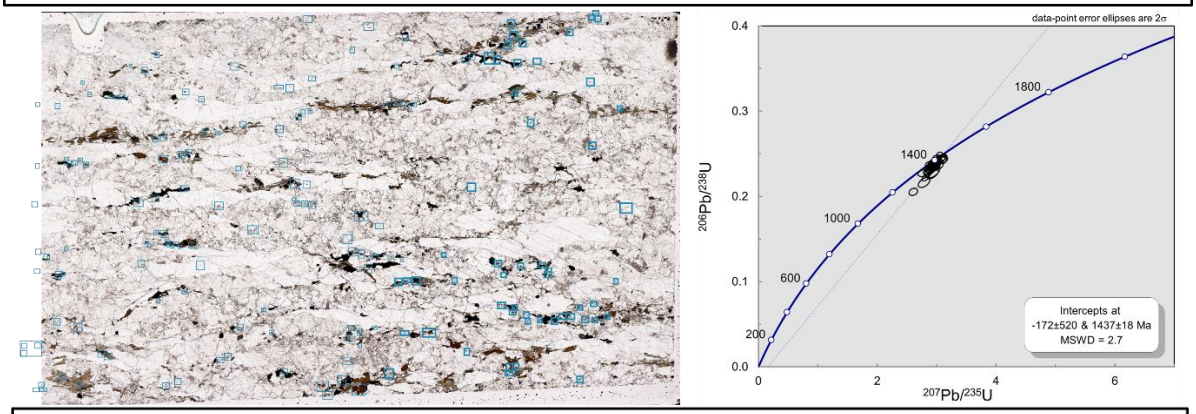

S22-07-2

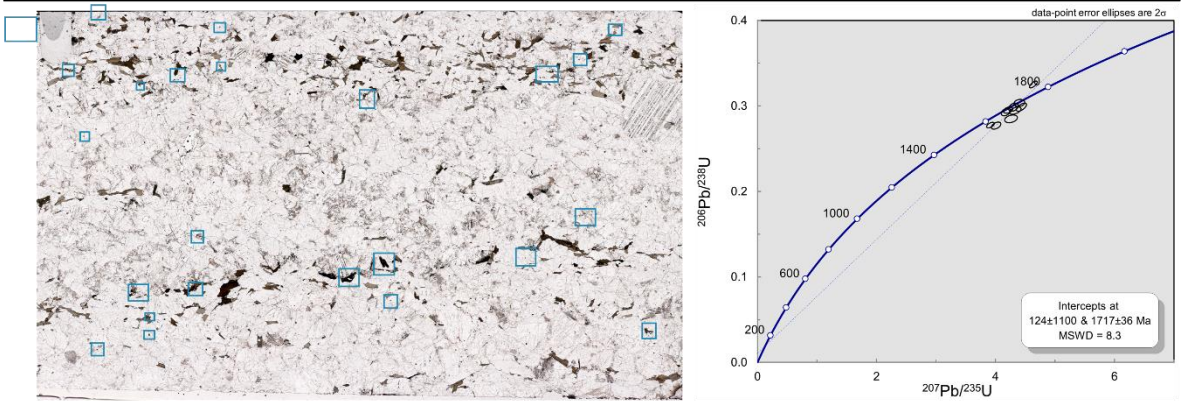

Figure 6: Zircon LA-ICP-MS geochronology results for 4 sites. Thin section scans are included with blue boxes denoting zircon locations. Concordia plots and weighted average plots for the dates included. Concordia data point error ellipses are 2σ.

S22-14

Zircon mineralization for S22-14 is proximal to biotite as well as hornblende which defines the foliation. Zircon grains are < 75 μm in maximum length and were predominantly between 20 – 50 μm. Samples S22-14-1 and S22-14-3 yielded average dates of 1464 ± 34 Ma and 1408 ± 15 Ma respectively. Dates collected for S22-14-1 ranged from 1390 Ma to 1491 Ma. For S22-14-3, dates ranged from 1335 Ma to 1450 Ma. These dates likely reflect the age of crystallization for the igneous intrusions, and this is also likely for samples S22-16 and S22-18.

S22-16

Zircon is more abundant in sample S22-16 when compared to the previous two sites, with larger zircon grains proximal to biotite and smaller grains found within the quartz and feldspar matrix. The majority of zircon grains are < 100 μm in size, however some grains are 150 – 200 μm. Sample S22-16 yielded an average date of 1445 ± 16 Ma but possesses a large MSWD compared to S22-14 and S22-18 which is likely related to Pb loss. Dates collected for S22-16 ranged 1379 Ma to 1548 Ma.

S22-18

Sample S22-18 possessed the most zircon compared to the other sites but also possessed the smallest grains. Most zircon grains are < 50 μm, with few between 50 – 75 μm. Zircon is more dispersed throughout this sample and was recorded along biotite foliation as well as within the quartz and feldspar matrix. Zircon minerals found along biotite grain boundaries are the larger of the mapped zircon and many grains found within the matrix were too small to be dated (< 20 μm). Sample S22-18 yielded an average date of 1437 ± 18 Ma. Dates collected for S22-18 ranged from 1373 Ma to 1504 Ma.

Monazite X-Ray Mapping

Ce, Y, Fe, and Mg maps were drafted for both S22-13 thin sections to better understand the relationship of rare earth elements (REE) within monazite, xenotime, and almandine garnet (Fig. 7). Garnet in our sample broke down as a result of decompression in the presence of melt which led to the reaction Grt + Sil + Qtz → Crd + Bt. Monazite and xenotime both occur within zones of garnet breakdown for both samples and monazite grains also appear as inclusions within garnet for S22-13-1.

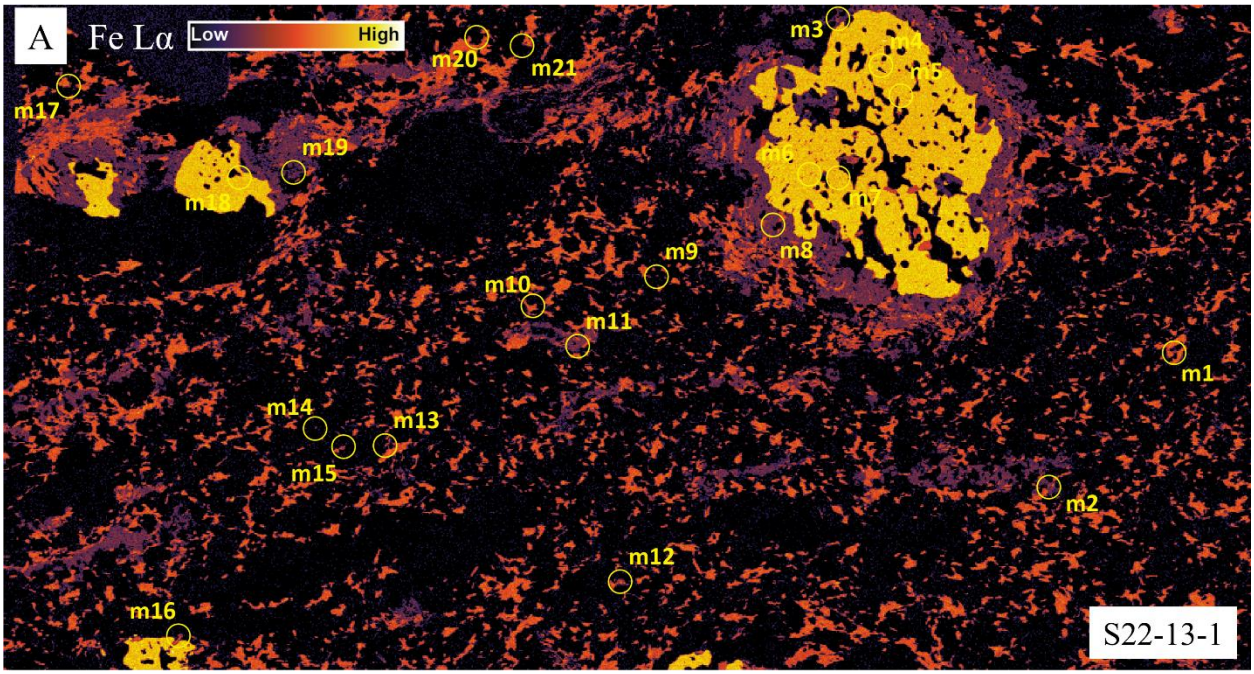

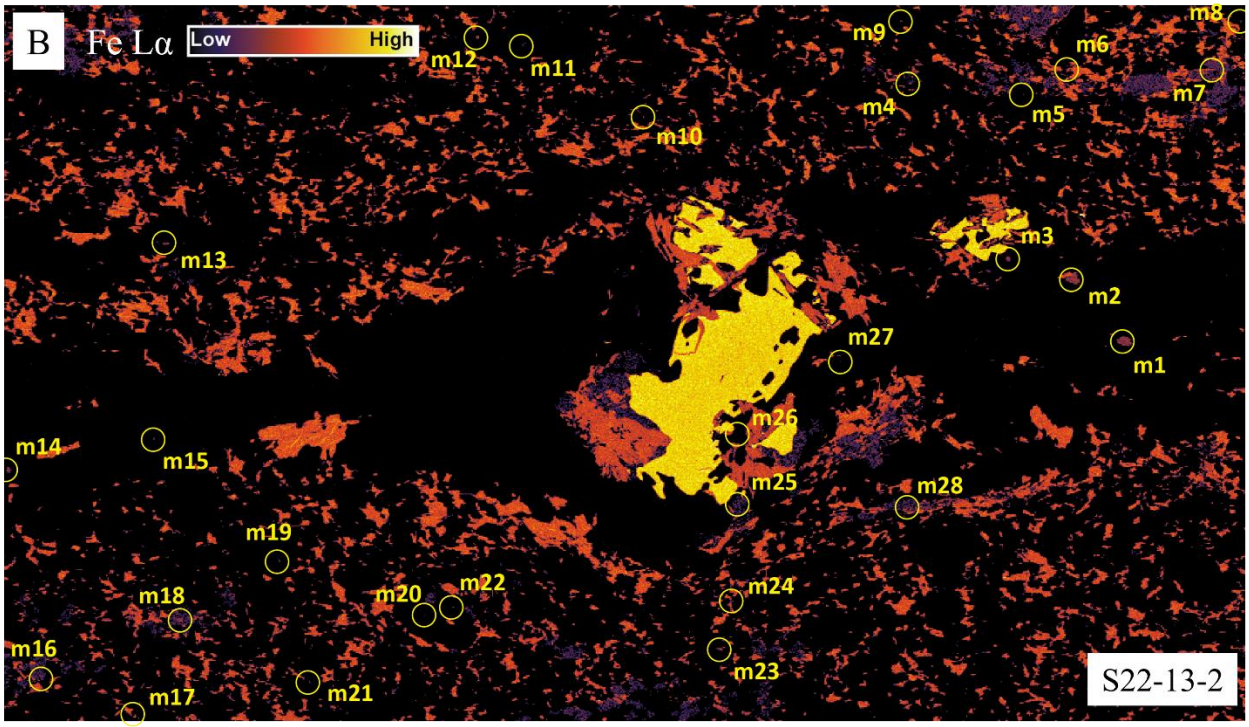

Figure 7: Fe Lα map with locations of monazite. [A] Map for sample S22-13-1. [B] Map for sample S22-13-2.

Whole Rock Analysis and Phase Equilibrium Modeling

Major and trace element concentrations for S22-13 are included in Table 2. Rare earth element data collected from sample S22-13 was normalized against REE values from Post Archean Australian Shale (PAAS) from Taylor and McLennan (1985). Normalized values for sample S22-13 were compared with normalized values for sample 090C, a garnet rich residue of metasediment melting from Athabasca, Canada (Fig. 8). Sample S22-13 possesses an Eu anomaly but otherwise plots near 1 with increasing values recorded for heavy rare earth elements (HREE).

Oxides		Trace Elements		Trace Elements	
Analyte Symbol	S22-13 (%)	Analyte Symbol	S22-13 (PPM)	Analyte Symbol	S22-13 (PPM)
SiO2	72.1	Sc	9	La	41.3
Al2O3	12.65	Be	3	Ce	87.1
Fe2O3	4.29	V	5	Pr	10.5
MnO	0.065	Cr	< 20	Nd	41.5
MgO	1.93	Co	3	Sm	9.2
CaO	1.8	Ni	< 20	Eu	2.26
Na2O	3.17	Cu	80	Gd	8.2
K2O	1.42	Zn	30	Tb	1.48
TiO2	0.314	Ga	15	Dy	9.46
P2O5	0.02	Ge	0.8	Ho	2
LOI	0.76	As	< 5	Er	6.26
Total	**98.52**	Rb	24	Tm	0.962
		Sr	91	Yb	6.79
		Y	55.5	Lu	1.06
		Zr	331	Hf	6.9
		Nb	16.6	Ta	1.12
		Mo	< 2	W	0.5
		Ag	< 0.5	Tl	0.11
		In	0.1	Pb	7
		Sn	3	Bi	< 0.1
		Sb	< 0.2	Th	7.64
		Cs	0.5	U	4.08
		Ba	398		

Table 2: Complete whole-rock analysis for S22-13 including major and trace elements.

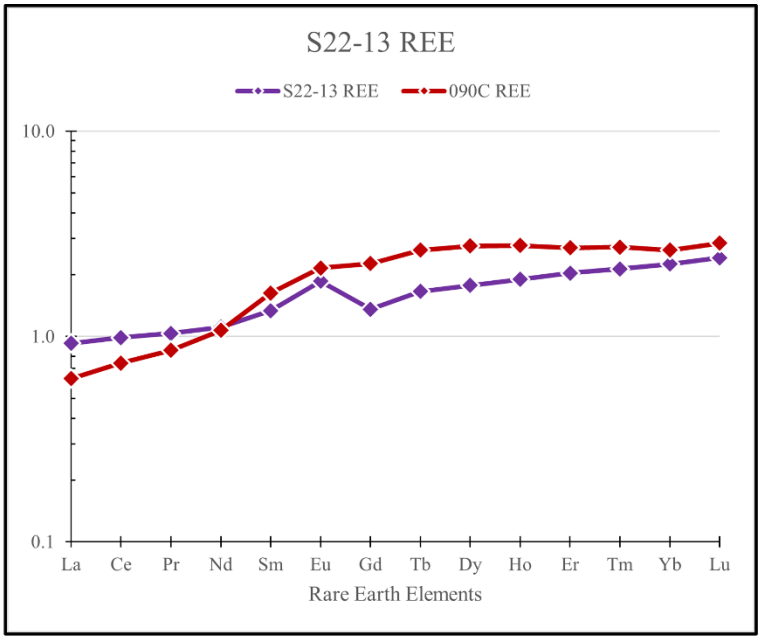

Figure 8: Rare earth element analysis for site S22-13. REE concentrations normalized against Post-Archean Australian Shale (PAAS) REE values. Purple data values represent site S22-13. Red data values represent sample 090C, a garnet rich residue of metasediment melting from Athabasca, Canada.

Sample S22-13 is a Grt + Sil + Crd + Bt + Kfs + Pl + Qtz metapelite migmatite with an assemblage that is appropriate for thermobarometry via phase equilibria modeling using Perple_X software, a Gibbs free energy minimization program (Connolly and Petrini, 2002; Connolly, 2005). Figure 9 shows the isochemical phase diagram model for this sample. The model was generated using the measured whole rock composition and assuming the H_2O content is equivalent to the loss on ignition. The actual amount was likely less if melting occurred in the absence of an external fluid. Due to fluid absent melting, the Melt-In side of Figure 9 is to be considered for the model.

Based on petrographic observations, the inferred peak metamorphic assemblage was Grt + Bt + Kfs + Sil + Melt. The stability field for this assemblage occurs at pressures > 0.55 GPa and < 0.65 GPa (Fig. 9). The presence of the solidus at > 700°C represents a minimum

temperature for this metamorphism (Fig. 9). The presence of cordierite as a corona around the perimeter of resorbed garnet within the samples suggests garnet breakdown via the divariant reaction Grt + Sil + Qtz → Crd or via the continuous reaction Grt + Kfs + Melt → Crd + Bt (Spear et al., 1999). This reaction results from cooling and crystallization, which leads to garnet resorbtion and the formation of cordierite, represented by the assemblage Grt + Bt + Kfs + Sil + Melt. The slope of this breakdown reaction implies decompression into cordierite stability may have been nearly isothermal (Fig. 9).

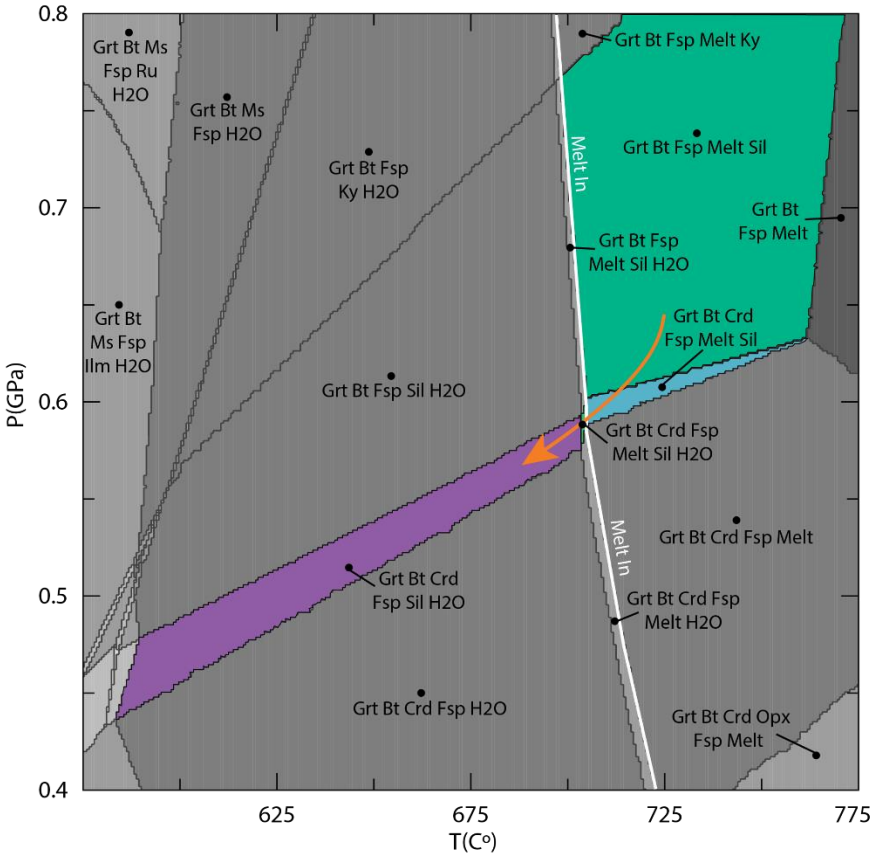

Figure 9: Thermobarometry phase equilibria model using Perple_X modeling software for site S22-13, a Grt + Sil + Crd + Bt + Kfs + Pl + Qtz migmatite. The green highlighted region indicates the inferred peak conditions for the sample represented by Grt + Bt + Fsp + Sil + Melt. The sample then underwent decompression and entered the lower pressure region represented by Grt + Bt + Crd + Fsp + Sil + Melt. Note that the model only applies to the Melt-In side of the diagram since melting was fluid-absent.

Discussion

The northeast-southwest striking foliation data collected in the field is consistent with data reported in previous studies and are indicative of north-northwest directed shortening during

the Mesoproterozoic (Boyer, 1962; Jones et al., 2010). The scatter of poles in the stereonet plots of Figure 3 imply folding at a regional scale (Fig. 4). Jones et al. (2010) inferred reverse-sense, north-northwest to south-southeast-directed crustal flow in the southern Wet Mountains. Only minor evidence for kinematics was observed in the field in this study, and it was opposite to previous studies, with normal-sense top-to-the-north sense of shear observed at site S22-14. This may or may not have occurred on the regional scale. Many of our samples display coarse recrystallization of minerals, predominantly through K-feldspar, plagioclase, and quartz. This recrystallization likely occurred post-deformation and led to annealing of these minerals and loss of evidence for kinematics. The regional shear sense of lower crustal flow preserved in the southern Wet Mountains remains difficult to confirm (Jones et al., 2010; Levine et al., 2013; this study).

All our samples, excluding S22-13, are composed of the lit-par-lit gneiss which possesses granitic to granodioritic magmas injected into the host metasedimentary rock sequences. These granites were emplaced at high temperatures and may have driven local metamorphism for the study area. A Paleoproterozoic date population is represented by S22-07 (1717 ± 36 Ma) which aligns with the plutonic population associated with the Garell Peak Pluton (1663 ± 4 Ma; 1666 ± 22 Ma; Bickford et al., 1989), the Crampton Mt. Pluton (1705 ± 8 Ma; Bickford et al., 1989), the Twin Mt. Pluton (1706 ± 5 Ma; Bickford et al., 1989), and the Mt. Tyndall Plutons (1615 ± 3 Ma; 1622 ± 5 Ma; 1653 ± 50 Ma; Bickford et al., 1989). The ~1700 Ma population of igneous intrusions aligns with current known Paleoproterozoic metamorphic events that extended across Arizona, New Mexico and Colorado (Karlstrom et al., 1987; Siddoway et al., 2000; Jones et al., 2010; Daniel et al., 2013; Aronoff et al., 2016). Deposition of sedimentary rocks (Site S22-07) is

determined to pre-date or be synchronous with emplacement of the Garell Peak Pluton and by association, Paleoproterozoic D1 reported by Jones et al. (2010).

The zircon dates derived from S22-14 (1408 ± 15 Ma; 1464 ± 34 Ma), S22-16 (1445 ± 16 Ma), and S22-18 (1437 ± 18 Ma) are interpreted to represent the age of crystallization for these magmas, aligning them with the Oak Creek Pluton (1439 ± 8 Ma; 1442 ± 7 Ma; Bickford et al., 1989) and W. McCoy Gulch Pluton (1460 ± 21 Ma; 1474 ± 7 Ma; Bickford et al., 1989) intrusion population. This younger population aligns with the Oak Creek Pluton, which is considered syntectonic with D_3. It is likely that the third deformation event coincides with the Picuris Orogen, which has largely been constrained between ~ 1480 Ma – 1350 Ma (Jones et al., 2011; Doe et al., 2012, 2013; Daniel et al., 2013; Aronoff et al., 2016; Holland et al., 2020; Mahatma et al., 2022; Daniel et al., 2022).

Rare earth element data from sample S22-13 suggests a shale-like protolith due to several elements plotting near 1 (La, Ce, Pr, Nd, Sm, Gd). The positive Eu anomaly could be a result from Eu substituting Ca in feldspar for this sample. The slight positive slope for HREE suggests enrichment as evidenced by the presence of abundant garnet in the sample. These results are consistent with other migmatite samples found near the Oak Creek pluton, which also recorded HREE enrichment (Hernández-Montenegro et al., 2019). For preservation of these rocks, melt loss is required which suggests syntectonic metamorphism and melting (White and Powell, 2002; Yakymchuk and Brown, 2014).

Microstructural analysis yielded observations that suggest minimum metamorphic conditions for the lit-par-lit gneiss. The presence of myrmekite, sericite, and quartz with chessboard extinction suggest temperatures > 650^{o}C. Monazite and xenotime occur in zones of

garnet breakdown and as inclusions within garnet for sample S22-13. In terms of monazite growth, it is likely that some monazite grains formed prior to garnet growth or developed during the prograde path of metamorphism, which is supported by the presence of monazite within the garnet. The xenotime grains that occur on the periphery of the resorbed garnet likely formed during decompression on the retrograde metamorphic path.

Pressure and temperature estimates for S22-13 suggest conditions > 700^{o}C and > 0.6 GPa, both of which are consistent with PT estimates presented by Hernández-Montenegro et al. (2019) of 750^{o}C and 0.7 GPa. Previous workers have interpreted the Wet Mountains to be a tilted segment of mid- to lower continental crust (Siddoway, et al., 2000; Jones et al., 2010), however the pressure and temperature conditions determined from the Hernández-Montenegro et al. (2019) study and our data suggest that the range is not tilted due to similar metamorphic and emplacement estimates (Fig. 10). This assists in understanding the history of the Wet Mountains, because it suggests that a large portion of the range was originally located in the middle crust and underwent similar metamorphic and deformative conditions throughout the range. In addition, site S22-07 confirms that sediments and sedimentary rocks were deposited during the Paleoproterozoic and then underwent burial to > 0.6 GPa likely during the Picuris Orogeny.

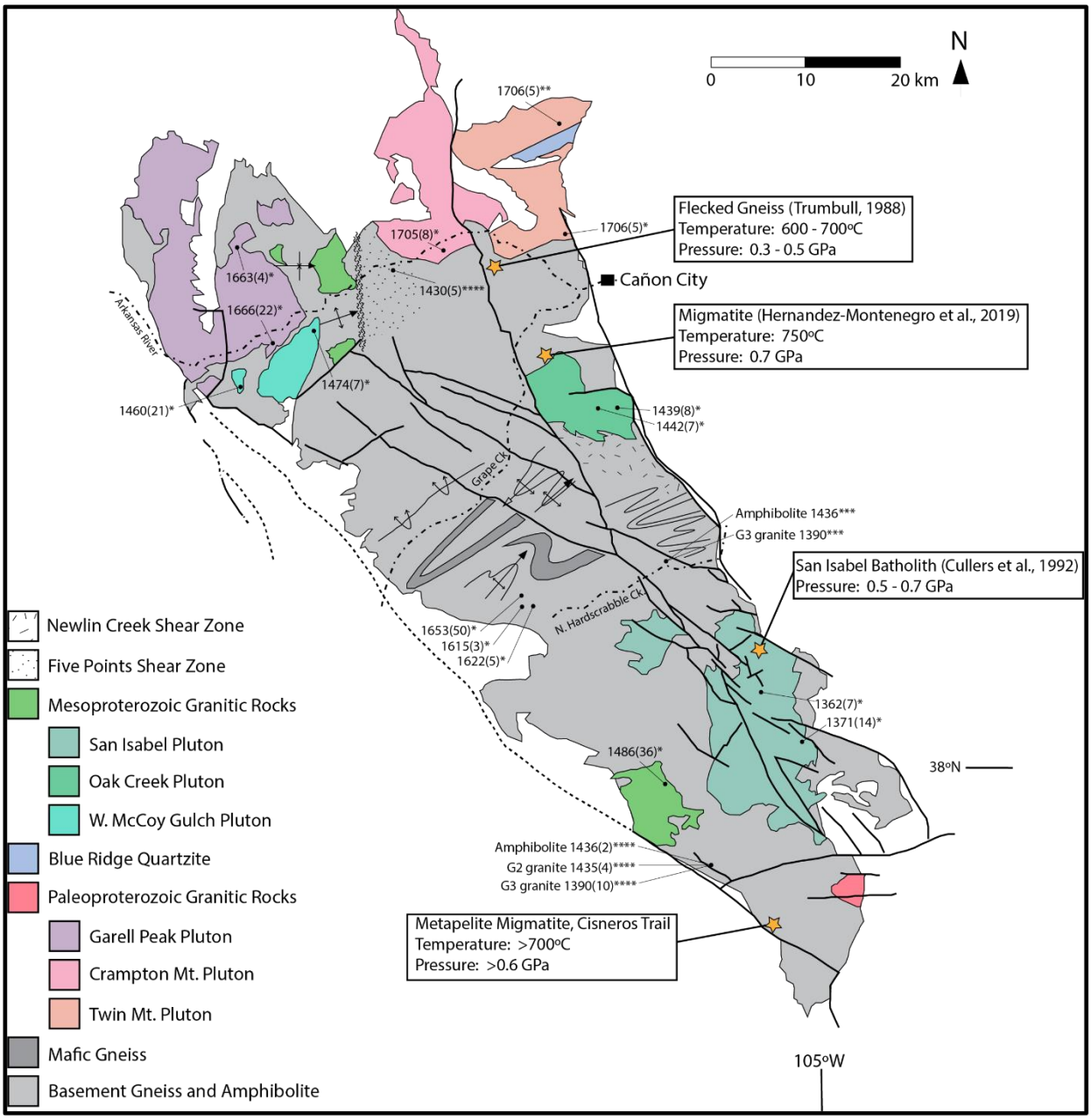

Figure 10: Proterozoic geologic map for the Wet Mountains, Colorado. Pressure-Temperature calculations for various regions of the Wet Mountains are marked with orange stars and associated data. Pressure and temperature conditions from Trumbull (1988), Cullers et al. (1992), and Hernandez-Montenegro et al. (2019). PT calculations for this study are in the southern range for the metapelite migmatite, Cisneros Trail. Map based on Tweto (1979), Bickford et al. (1989), Siddoway et al. (2000), and Jones et al. (2010). U-Pb geochronology of Bickford et al. (1989)*, Jones et al. (2009)**, Jones (2005)***, Jones (2010)****.

Conclusions

This study investigated the deformation and metamorphism of the southern Wet Mountains which possesses implications for the regional extent of the Picuris Orogeny. Samples from this study were collected from lit-par-lit gneiss and possessed dates in accordance with Mesoproterozoic granitic intrusions that are suggested to be syn-tectonic with respect to third deformation event. Pressure and temperature calculations for sample S22-13 determined inferred peak conditions > 700^{o}C and > 0.6 GPa, which corresponds with other pressure and temperature estimates in the central Wet Mountains. The oldest sample from this study provided evidence for deposition of Paleoproterozoic sediments that were displaced to > 0.6 GPa. This displacement is likely the result of the regional Mesoproterozoic Picuris orogenic event.

References

Amato, J.M., Boullion, A.O., Serna, A.M., Sanders, A.E., Farmer, G.L., Gehrels, G.E., Wooden, J.L., 2008. Evolution of the Mazatzal province and the timing of the Mazatzal orogeny: Insights from U-Pb geochronology and geochemistry of igneous and metasedimentary rocks in southern New Mexico: GSA Bulletin, 120(3-4): 328-346. https://doi.org/10.1130/B26200.1

Aronoff, R.F., Andronicos, C.L., Vervoort, J.D., Hunter, R.A., 2016. Redefining the metamorphic history of the oldest rocks in the southern Rocky Mountains: GSA Bulletin, 12(7-8): 1207-1227. https://doi.org/10.1130/B31455.1

Bickford, M.E., Cullers, R.L., Shuster, R.D., Premo, W.R., Van Schmus, W.R., 1989. U-Pb zircon geochronology of Proterozoic and Cambrian plutons in the Wet Mountains and southern Front Range, Colorado: GSA Special Papers; Proterozoic Geology of the Southern Rocky Mountains. https://doi.org/10.1130/SPE235

Boyer, R.E., 1962. Petrology and Structure of the Southern Wet Mountains, Colorado: GSA Bulletin, 73(9): 1047-1070. https://doi.org/10.1130/0016-7606(1962)73[1047:PASOTS]2.0.CO;2

Connolly, J.A.D., 1995. PeRpLeX: A Tutorial: Perple_X Documentation. https://www.perplex.ethz.ch/perplex_documentation.html#Web-based_Documentation

Connolly, J.A.D., Petrini, K., 2002. An automated strategy for calculation of phase diagram sections and retrieval of rock properties as a function of physical conditions: Journal of Metamorphic Geology, 20(7): 697-708.

Connolly, J.A.D., 2005. Computation of phase equilibria by linear programming: A tool for geodynamic modeling and its application to subduction zone decarbonation: Earth and Planetary Science Letters, 236(1-2): 524-541. https://doi.org/10.1016/j.epsl.2005.04.033.

Cullers, R.L., Griffin, T., Bickford, M.E., Anderson, J.L., 1992. Origin and chemical evolution of the 1360 Ma San Isabel batholith, Wet Mountains, Colorado: A mid-crustal granite of anorogenic affinities: GSA Bulletin, 104(3): 316-328. https://doi.org/10.1130/0016-7606(1992)104%3C0316:OACEOT%3E2.3.CO;2

Daniel, C.G., Pfeifer, L.S., Jones III, J.V., McFarlane, C.M., 2013. Detrital zircon evidence for non-Laurentian provenance, Mesoproterozoic [ca. 1490-1450 Ma] deposition and orogenesis in a reconstructed orogenic belt, northern New Mexico, USA: Defining the Picuris orogeny: GSA Bulletin, 125(9-10): 1423-1441. https://doi.org/10.1130/B30804.1

Daniel, C.G., Indares, A., Medaris, L.G., Aronoff, R., Malone, D., Schwartz, J., 2022. Linking the Pinware, Baraboo, and Picuris orogens: Recognition of a trans-Laurentian ca. 1520-1340 Ma orogenic belt *in* Whitmeyer, S. J., Williams, M. L., Kellett, D. A., and Tikoff, B., 2022. Laurentia: Turning Points in the Evolution of a Continent: Geological Society of America Memoir 220. https://doi.org/10.1130/2022.1220(11)

Doe, M.F., Jones III, J.V., Karlstrom, K.E., Thrane, K., Frei, D., Gehrels, G., Pecha, M., 2012. Basin formation near the end of the 1.60-1.45 Ga tectonic gap in southern Laurentia: Mesoproterozoic Hess Canyon Group of Arizona and implications for ca. 1.5 Ga supercontinent configurations: Lithosphere, 4(1): 77-88. https://doi.org/10.1130/L160.1

Doe, M.F., Jones III, J.V., Karlstrom, K.E., Dixon, B., Gehrels, G., Pecha, M., 2013. Using detrital zircon ages and Hf isotopes to identify 1.48-1.45 Ga sedimentary basins and fingerprint sources of exotic 1.6-1.5 Ga grains in southwestern Laurentia: Precambrian Research. https://doi.org/10.10106/j.precamres.2013.03.002.

Dumond, G., Mahan, K.H., Goncalves, P., Williams, M.L., Jercinovic, J., 2022. Monazite as a monitor of shear strain in orogenic crust: Journal of Structural Geology, 161. https://doi.org/10.1016/j.jsg.2022.104672

Hernández-Montenegro, D., Andronicos, C.L., Zuluaga, C.A., Aronoff, R.F., 2019. Effects of melt loss, melt retention, and protolith composition on differentiation of anatectic metapelites: A case study of the Wet Mountains, Colorado: Lithos, 344-345: 425-439. https://doi.org/10.1016/j.lithos.2019.06.032.

Holland, T., Powell, R., 2003. Activity-composition relations for phases in petrological calculations: an asymmetric multicomponent formulation: Contributions to Mineralogy and Petrology, 145: 492-501. https://doi.org/10.1007/s00410-003-0464-z

Holland, M.E., Grambling, T.A., Karlstrom, K.E., Jones III, J.V., Nagotko, K.N., Daniel, C.G., 2020. Geochronologic and Hf-isotope framework of Proterozoic rocks from central New Mexico, USA: Formation of the Mazatzal crustal province in an extended continental margin arc: Precambrian Research, 347. https://doi.org/10.1016/j.precamres.2020.105820

Jones III, J.V., Siddoway, C.S, Connelly, J.N., 2010. Characteristics and implications of ca. 1.4 Ga deformation across a Proterozoic mid-crustal section, Wet Mountains, Colorado, USA: Lithosphere, 2(2): 119-135. https://doi.org/10.1130/L78.1

Jones III, J.V., Daniel, C.G., Frei, D., Thrain, K., 2011. Revised regional correlations and tectonic implications of Paleoproterozoic and Mesoproterozoic metasedimentary rocks in northern New Mexico, USA: New findings from detrital zircon studies of the Hondo Group, Vadito Group, and Marqueñas Formation: Geosphere, 7(4): 974-991. https://doi.org/10.1130/GES00614.1

Karlstrom, K.E., Bowring, S.A., Conway, C.M., 1987. Tectonic significance of an early Proterozoic two-province boundary in central Arizona: GSA Bulletin, 99(4): 529-538. https://doi.org/10.1130/0016-7606(1987)99<529:TSOAEP>2.0CO;2

Karlstrom, K.E., Bowring, S.A., 1988. Early Proterozoic assembly of tectonostratigraphic terranes in southwestern North America: Journal of Geology, 96(5): 561-576. https://doi.org/10.1086/629252

Karlstrom, K.E., Dallmeyer, D., Grambling, J.A., 1997. $^{40}Ar/^{39}Ar$ evidence for 1.4 Ga regional metamorphism in New Mexico: Implications for thermal evolution of the lithosphere in the

southwestern U.S.A.: The Journal of Geology, 105(2): 205-224. https://doi.org/10.1086/515912

Karlstrom, K.E., Ahall, K.I., Harlan, S.S., Williams, M.L., McLelland, J., and Geissman, J.W., 2001. Long-lived (1.8-1.0 Ga) convergent orogen in southern Laurentia, its extensions to Australia and Baltica, and implications for refining Rodinia: Precambrian Research, v. 111, p. 5-30. https://doi.org/10.1016/S0301-9268(01)00154-1

Levine, S.F., Mosher, S., Siddoway, C.S., 2013. Relationship between syndeformational partial melting and crustal-scale magmatism and tectonism across the Wet Mountains, central Colorado: Lithosphere, 5(5): 456-476. https://doi.org/10.1130/L287.1

Mahatma, A.A., Kuiper, Y.D., Holm-Denoma, C.S., 2022. Evidence for the ~1.4 Ga Picuris orogeny in the central Colorado Front Range: Precambrian Research, 382. https://doi.org/10.1016/j.precamres.2022.106878

Nyman, M.W., Karlstrom, K.E., Kirby, E., Graubard, C.M., 1994. Mesoproterozoic contractional orogeny in western North America: Evidence from ca. 1.4 Ga plutons: Geology, 22(10): 901-904. https://doi.org/10.1130/0091-7613(1994)022%3C0901:MCOIWN%3E2.3.CO;2

Trumbull, R.B., 1988. Petrology of flecked gneisses in the northern Wet Mountains, Fremont County, Colorado: GSA Bulletin, 100(2): 247-256. https://doi.org/10.1130/0016-7606(1988)100%3C0247:POFGIT%3E2.3.CO;2

Siddoway, C.S., Givot, R.M., Bodle, C.D., Heizler, M.T., 2000. Dynamic versus anorogenic setting for Mesoproterozoic plutonism in the Wet Mountains, Colorado: Does the interpretation depend on level of exposure: Rocky Mountain Geology, 35(1): 91-111. https://doi.org/10.2113/35.1.91

Silver, L.T., 1965. Mazatzal orogeny and tectonic episodicity, Abstracts for 1964: Boulder, Colorado, Geological Society of America Special Paper 82, p. 185-188.

Spear, F., Kohn, M., Cheney, J., 1999. P-T paths from anatectic pelites: Contributions to Mineralogy and Petrology, 134: 17-32. https://doi.org/10.1007/s004100050466

Taylor, S.R., McLennan, S.M., 1985. The continental crust: Its composition and evolution. United States.

White, R.W., Powell, R., Holland, T.J.B., Worley, C.C., 2000. The effect of TiO_2 and Fe_2O_3 on metapelitic assemblages at greenschist and amphibolite facies conditions: mineral equilibria calculations in the system K_20-FeO-MgO-Al_2O_3-SiO_2-H_2O-TiO_2-Fe_2O_3: Journal of Metamorphic Geology, 18: 497-511. https://doi.org/10.1046/j.1525-1314.2000.00269.x

White, R.W., Powell, R., 2002. Melt loss and preservation of granulite facies mineral assemblages: Journal of Metamorphic Geology, 20(7): 621-632. https://doi.org/10.1046/j.1525-1314.2002.00206_20_7.x

White, R.W., Powell, R., Holland, T.J.B., Johnson, T.E., Green, E.C.R., 2014. New mineral activity-composition relations for thermodynamic calculations in metapelitic systems: Journal of Metamorphic Geology, 32: 261-286. https://doi.org/10.1111/jmg.12071

Williams, M.L., Jercinovic, M.J., Mahan, K.H., Dumond, G., 2017. Electron Microprobe Petrochronology: Reviews in Mineralogy and Geochemistry, 83: 153-182. https://doi.org/10.2138/rmg.2017.83.5

Yakymchuk, C., Brown, M., 2014. Consequences of open-system melting in tectonics: Journal of the Geological Society, London, 171(1): 21-40. https://doi.org/10.1144/jgs2013-039

Appendix A: LA-ICP-MS U-Pb Zircon Analytical Data Southern Wet Mountains

Sample Analysis	$^{207}Pb/^{235}U$	2σ error	$^{206}Pb/^{238}U$	2σ error	$^{206}Pb/^{238}U$ versus $^{207}Pb/^{235}U$	$^{238}U/^{206}Pb$ Date	2σ error	$^{207}Pb/^{206}Pb$ Date	2σ error	$^{207}Pb/^{206}Pb$ versus $^{238}U/^{206}Pb$
S22-07-2										
S22-07-2_4.5	4.4366408	0.0702456	0.2985551	0.0039133	0.6276553	1683.53	19.31	1772.46	29.72	0.035828096
S22-07-2_4.8a_core	4.3322152	0.0797368	0.2945765	0.0035115	0.4896082	1664.10	17.54	1734.48	29.99	0.180744933
S22-07-2_4.9	3.9165105	0.0538523	0.2775208	0.0026390	0.5682780	1578.53	13.29	1677.35	23.34	0.111200103
S22-07-2_4.10a	4.3018434	0.0662092	0.2985153	0.0039294	0.3652481	1683.46	19.47	1719.61	31.37	0.389649924
S22-07-2_4.10b	4.2630539	0.0873992	0.2849371	0.0037596	0.3181830	1615.80	18.88	1773.21	40.60	0.30805524
S22-07-2_4.12	4.4031185	0.0742038	0.3036031	0.0033988	0.1616147	1708.60	16.79	1716.25	34.06	0.451894156
S22-07-2_4.13	4.0090350	0.0654052	0.2768773	0.0033746	0.4692169	1575.18	17.04	1708.52	31.03	0.341623851
S22-07-2_4.19a	4.1749378	0.0640862	0.2928827	0.0036740	0.4009796	1655.29	18.03	1694.75	26.57	0.219117359
S22-07-2_4.21	4.2116652	0.0628228	0.2952213	0.0029454	0.3762043	1667.21	14.64	1691.19	27.70	0.279293729
S22-07-2_4.23	4.6373228	0.0527414	0.3251084	0.0033280	0.7217437	1814.34	16.20	1683.21	15.89	0.309394748
S22-14-1										
S22-14-1_4.1c	2.9985188	0.0679403	0.2421175	0.0032148	0.4034430	1397.13	16.65	1416.21	37.58	0.196099327
S22-14-1_4.1b	3.0784666	0.0636317	0.2403922	0.0035447	0.2295420	1388.12	18.38	1462.46	38.25	0.503164703
S22-14-1_4.2a	3.0649056	0.0648519	0.2389707	0.0027806	0.1405744	1381.02	14.47	1475.21	43.98	0.398736648
S22-14-1_4.3h	2.9136858	0.0714969	0.2359614	0.0032077	0.2704999	1365.11	16.68	1406.50	46.45	0.278312097
S22-14-1_4.6	3.0555437	0.0653292	0.2465788	0.0036878	0.4403411	1420.11	19.01	1419.22	46.74	0.252803922
S22-14-1_4.9a	3.0383655	0.0632189	0.2418792	0.0030067	0.2273860	1396.06	15.62	1449.51	44.59	0.334624879
S22-14-1_4.9b	2.8537741	0.0585977	0.2249944	0.0039129	0.1563795	1307.74	20.60	1468.21	47.53	0.58055057
S22-14-1_4.12a	2.9156757	0.0577569	0.2355265	0.0027050	0.2027922	1363.04	14.11	1410.69	38.13	0.377899206
S22-14-1_4.14_core	3.1631299	0.0773492	0.2511674	0.0039051	0.4067895	1444.04	20.16	1469.32	35.40	0.249300952
S22-14-1_4.17e	3.1444433	0.0995633	0.2462232	0.0058969	0.3932135	1418.32	30.50	1491.29	60.27	0.352864359
S22-14-1_4.17c	2.8547351	0.0621310	0.2231791	0.0034943	0.3250317	1297.94	18.38	1467.08	42.55	0.242649198
S22-14-1_4.17g	3.0026897	0.0587674	0.2349558	0.0025649	0.2243292	1362.33	14.06	1463.08	39.48	0.334668649
S22-14-1_4.18	3.0222750	0.0622244	0.2448989	0.0035360	0.0638249	1411.47	18.17	1409.52	45.83	0.663401445
S22-14-1_4.21a	2.9835014	0.0750006	0.2403340	0.0030339	0.3401638	1387.95	15.74	1408.97	46.61	0.176647468
S22-14-1_4.23a_core	3.1905068	0.0784682	0.2494730	0.0035768	0.2584913	1435.10	18.47	1467.02	47.82	0.315144815
S22-14-1_4.25	2.9731802	0.0648753	0.2390571	0.0029671	0.1722741	1381.33	15.38	1416.70	44.16	0.408116545
S22-14-1_4.27a	2.8984544	0.0438787	0.2308489	0.0025653	0.3058732	1338.60	13.43	1441.39	30.34	0.369269758
S22-14-1_4.28a	3.0817757	0.0538227	0.2433203	0.0026401	0.3606892	1403.57	13.69	1456.18	32.52	0.261657268
S22-14-1_4.28c	2.9100177	0.0698461	0.2278996	0.0030779	0.4584029	1323.15	16.10	1462.05	52.50	0.163747203
S22-14-1_4.29a	2.8009803	0.0525739	0.2242133	0.0040490	0.6481321	1303.30	21.30	1431.05	29.48	0.39549101
S22-14-1_4.31a	2.8482774	0.0369718	0.2334686	0.0022946	0.3659720	1352.41	11.99	1390.92	25.00	0.370255466
S22-14-1_4.36a	3.1115899	0.0419750	0.2422440	0.0025583	0.3813950	1398.01	13.27	1484.86	27.94	0.388466288
S22-14-1_4.39b	2.8380868	0.0548515	0.2271498	0.0030028	0.2430599	1319.06	15.77	1437.71	41.53	0.379852415
S22-14-3										
S22-14-3_4.2a	2.8847670	0.0711951	0.2360794	0.0043613	0.2880105	1365.20	22.64	1400.45	42.95	0.39146064
S22-14-3_4.3a	2.9879078	0.0692081	0.2425295	0.0028371	0.2581525	1399.48	14.70	1394.81	45.04	0.260292585
S22-14-3_4.5a	2.9902381	0.0858468	0.2437833	0.0041064	0.2458081	1405.38	21.20	1375.74	59.55	0.310892681
S22-14-3_4.7	2.8755720	0.0773547	0.2421389	0.0031601	0.0475756	1397.42	16.39	1335.66	57.53	0.412806287
S22-14-3_4.12	2.9550057	0.0633947	0.2426562	0.0033036	0.1539013	1399.93	17.15	1379.47	45.03	0.443703056
S22-14-3_4.14	2.8822991	0.0481923	0.2327634	0.0030295	0.1891100	1348.46	15.83	1418.92	36.03	0.446068422
S22-14-3_4.19a	2.9839600	0.0612071	0.2410874	0.0027954	0.4933176	1391.94	14.51	1411.95	39.48	0.14195717
S22-14-3_4.19b	3.0213268	0.0531168	0.2453887	0.0031661	0.3427941	1414.13	16.36	1410.36	35.54	0.326619315
S22-14-3_4.23	2.9104258	0.0591836	0.2377159	0.0030086	0.0729365	1374.27	15.60	1392.30	36.10	0.368846106
S22-14-3_4.27c	3.0396958	0.0745725	0.2423084	0.0031174	0.1886776	1398.25	16.15	1450.68	46.16	0.334812828
S22-14-3_4.28c	2.9566644	0.0744904	0.2421671	0.0030869	0.1541790	1397.43	16.02	1384.87	51.59	0.325237897
S22-14-3_4.28d	3.0344396	0.0554977	0.2465209	0.0028372	0.2398920	1420.07	14.65	1406.55	38.27	0.126088813

Appendix A: LA-ICP-MS U-Pb Zircon Analytical Data Southern Wet Mountains (Continued)

Sample Analysis	$^{207}Pb/^{235}U$	2σ error	$^{206}Pb/^{238}U$	2σ error	$^{206}Pb/^{238}U$ versus $^{207}Pb/^{235}U$	$^{238}U/^{206}Pb$ Date	2σ error	$^{207}Pb/^{206}Pb$ Date	2σ error	$^{207}Pb/^{206}Pb$ versus $^{238}U/^{206}Pb$
S22-16										
S22-16_4.1	3.1109272	0.0677634	0.2384634	0.0028828	0.2527909	1378.27	15.00	1497.71	43.79	0.279067731
S22-16_4.2	2.0730973	0.1289215	0.1567578	0.0099794	0.9481850	932.72	55.33	1539.90	30.83	0.350571199
S22-16_4.3	3.0251723	0.0707677	0.2383770	0.0045902	0.7346428	1377.15	23.87	1465.63	32.26	0.184473955
S22-16_4.5b	3.1333149	0.0604075	0.2550159	0.0031653	0.3340098	1463.78	16.29	1387.98	37.19	0.337310129
S22-16_4.7a	2.9134898	0.0491706	0.2357018	0.0029480	0.2345725	1363.85	15.35	1403.42	31.97	0.084917126
S22-16_4.7b	2.9100657	0.0478893	0.2325903	0.0029825	0.2660740	1347.59	15.59	1429.53	35.77	0.463788173
S22-16_4.7d	2.3967787	0.1067124	0.1868893	0.0096002	0.9157162	1099.23	52.15	1500.38	35.37	0.589181804
S22-16_4.7e	2.9701545	0.0456742	0.2377254	0.0025540	0.4967758	1374.52	13.28	1418.14	28.01	0.268313712
S22-16_4.8	3.0495738	0.0490962	0.2425719	0.0028391	0.1568573	1402.03	14.04	1432.03	33.59	0.265248843
S22-16_4.9b	3.0120779	0.0488968	0.2438218	0.0032799	0.4338370	1405.97	17.01	1404.66	33.38	0.438191867
S22-16_4.10f	2.9519207	0.0781882	0.2291192	0.0030357	0.3321512	1329.60	15.95	1468.90	47.04	0.168366436
S22-16_4.11a	2.9353788	0.0640799	0.2305805	0.0030278	0.3180869	1337.05	15.87	1449.66	41.82	0.302575536
S22-16_4.11b	2.9315020	0.0687486	0.2352211	0.0034739	0.1348639	1361.17	18.11	1421.34	50.46	0.298317372
S22-16_4.12	2.9615936	0.0661491	0.2338420	0.0032775	0.4673723	1354.04	17.10	1445.46	37.90	0.17916542
S22-16_4.13	3.0793081	0.0369674	0.2455447	0.0027498	0.3625915	1415.07	14.19	1437.74	25.09	0.510933862
S22-16_4.15b	3.0472475	0.0718213	0.2417562	0.0049005	0.4051815	1395.22	25.34	1444.11	47.84	0.460959866
S22-16_4.15c	2.7680647	0.0817058	0.2203542	0.0061171	0.6084251	1282.42	32.18	1441.78	46.98	0.337382868
S22-16_4.18	2.8141084	0.0795993	0.2312054	0.0047042	0.4794134	1339.65	24.45	1366.24	58.18	-0.025592417
S22-16_4.20a	2.9003705	0.0454831	0.2346122	0.0034976	0.5028041	1357.98	18.14	1417.42	26.33	0.397776283
S22-16_4.21	2.9149552	0.0633328	0.2374835	0.0033975	0.1949266	1372.99	17.67	1391.76	42.34	0.023586475
S22-16_4.22	2.8904729	0.0661914	0.2301956	0.0041300	0.6696143	1334.61	21.74	1432.29	32.38	0.197455439
S22-16_4.23	2.9510356	0.0519595	0.2352766	0.0030890	0.2524199	1361.59	16.13	1433.68	35.03	0.465335252
S22-16_4.24	3.0267850	0.0605747	0.2364607	0.0031791	0.5096553	1367.74	16.54	1463.77	32.61	0.117312468
S22-16_4.25a_core	2.4159320	0.1100489	0.1854704	0.0093442	0.9373156	1091.69	51.50	1522.00	35.84	0.592911595
S22-16_4.25c	2.7410646	0.0545628	0.2215428	0.0028027	0.2027762	1289.60	14.76	1402.50	34.64	0.17296478
S22-16_4.26	3.1119947	0.1331634	0.2392326	0.0058695	0.1003085	1380.88	30.58	1474.28	91.44	0.397820357
S22-16_4.38	2.3299795	0.1138418	0.1826299	0.0102518	0.9418896	1075.26	55.98	1488.14	34.74	0.516871296
S22-16_4.43	3.0285665	0.0541312	0.2284526	0.0033245	0.5621822	1325.80	17.40	1548.41	30.45	0.265947705
S22-16_4.45a	2.9747176	0.0630244	0.2393274	0.0032127	0.4736684	1382.66	16.72	1404.58	33.95	-0.002098739
S22-16_4.45b	2.9284937	0.0581747	0.2403972	0.0033189	0.5835023	1391.20	18.23	1379.40	31.24	0.180480152
S22-16_4.46a	3.1027725	0.0721318	0.2462357	0.0031930	0.3792403	1418.51	16.49	1438.19	43.17	0.162887203
S22-16_4.46c	3.0945980	0.0552274	0.2406671	0.0024813	0.2346112	1389.84	12.87	1477.67	34.39	0.315966602
S22-16_4.48	2.9026788	0.0436265	0.2345726	0.0033273	0.3275187	1357.83	17.37	1414.56	32.82	0.473391919
S22-16_4.49	3.0292380	0.0589618	0.2383191	0.0034675	0.5412022	1377.32	17.98	1458.11	33.75	0.219867939

Appendix A: LA-ICP-MS U-Pb Zircon Analytical Data Southern Wet Mountains (Continued)

Sample Analysis	$^{207}Pb/^{235}U$	2σ error	$^{206}Pb/^{238}U$	2σ error	$^{206}Pb/^{238}U$ versus $^{207}Pb/^{235}U$	$^{238}U/^{206}Pb$ Date	2σ error	$^{207}Pb/^{206}Pb$ Date	2σ error	$^{207}Pb/^{206}Pb$ versus $^{238}U/^{206}Pb$
S22-18										
S22-18_4.3	2.9751809	0.0621025	0.2393449	0.0028548	0.1375580	1382.86	14.85	1411.52	42.02	0.145731344
S22-18_4.8	2.8920321	0.0605431	0.2345786	0.0033120	0.4294047	1357.88	17.26	1405.46	34.89	0.231460475
S22-18_4.14a	2.9595272	0.0723336	0.2365195	0.0044048	0.2738935	1367.70	22.86	1424.40	46.94	0.381792777
S22-18_4.18a	2.7877680	0.0799783	0.2163015	0.0048860	0.5089823	1261.33	25.77	1482.54	46.55	0.336184484
S22-18_4.31a	2.9389210	0.0520083	0.2380780	0.0035871	0.3951642	1376.02	18.62	1393.60	35.66	0.455836342
S22-18_4.31b	2.9181803	0.0495421	0.2327716	0.0023455	0.1961532	1348.72	12.27	1431.31	34.63	0.370852092
S22-18_4.53b	3.0457356	0.0401920	0.2486966	0.0027055	0.3651698	1431.40	13.95	1390.30	25.79	0.486379349
S22-18_4.54a	2.7791480	0.0784780	0.2275726	0.0034446	0.3151507	1321.17	18.08	1373.07	48.44	0.093456377
S22-18_4.61e	2.9742479	0.0643263	0.2339785	0.0034695	0.3807044	1354.62	18.22	1449.26	40.71	0.297012406
S22-18_4.79a	2.9018417	0.0430052	0.2360073	0.0029404	0.5733004	1365.45	15.32	1394.85	23.27	0.357626396
S22-18_4.89b	3.0652743	0.0647620	0.2426759	0.0029322	0.5120681	1400.15	15.19	1441.64	41.65	0.062528203
S22-18_4.91a	3.0174547	0.0540065	0.2413244	0.0030427	0.2792936	1393.09	15.80	1421.69	35.69	0.326835763
S22-18_4.91b	2.9554437	0.0809000	0.2280071	0.0049204	0.6706201	1322.73	25.93	1499.85	35.85	0.177063097
S22-18_4.102a	2.8766690	0.0606569	0.2323259	0.0033388	0.5732832	1346.08	17.50	1420.47	33.06	0.110730329
S22-18_4.106	2.9405591	0.0734572	0.2259112	0.0044911	0.6943701	1311.81	23.86	1504.12	33.44	0.236223142
S22-18_4.109	3.0091483	0.0522246	0.2393306	0.0025997	0.5487752	1382.86	13.50	1444.74	30.18	0.013296331
S22-18_4.114a	2.9040329	0.0445913	0.2348503	0.0025984	0.3265729	1359.51	13.57	1398.76	28.74	0.4412601
S22-18_4.116d	3.0093629	0.0425317	0.2386910	0.0024711	0.2440940	1379.57	12.85	1451.00	29.47	0.505331903
S22-18_4.123a	2.8810903	0.0528029	0.2306005	0.0025662	0.2347001	1337.29	13.44	1430.71	35.24	0.347183159
S22-18_4.135	3.0034005	0.0630564	0.2421001	0.0047116	0.6456843	1396.92	24.37	1424.88	31.73	0.291728444
S22-18_4.158	2.9434385	0.0447359	0.2380956	0.0025631	0.2738269	1376.44	13.34	1407.90	30.95	0.405555569
S22-18_4.168a	2.6068236	0.0593864	0.2053777	0.0034861	0.2471852	1203.47	18.67	1454.37	33.53	0.474953758
S22-18_4.169	3.0025711	0.0584740	0.2449416	0.0029059	0.1933094	1411.90	15.05	1383.52	40.68	0.405337737
S22-18_4.175	2.9509489	0.0439967	0.2414876	0.0029115	0.3648139	1393.98	15.14	1390.27	30.39	0.357248774
S22-18_4.4L_c	2.8163108	0.0515660	0.2221219	0.0033081	0.5818600	1292.48	17.50	1459.48	28.32	0.241038475
S22-18_4.4L_f	2.9896016	0.0411930	0.2341344	0.0026987	0.2382202	1355.75	14.06	1475.20	29.87	0.478891436
S22-18_4.6L_a	3.0805994	0.0858253	0.2437621	0.0038866	0.1425492	1405.44	20.13	1437.12	58.18	0.411716906
S22-18_4.6L_c	2.9618013	0.0561447	0.2361035	0.0033482	0.3384726	1365.82	17.40	1442.10	40.30	0.320102358
S22-18_4.6L_d	3.0019093	0.0543272	0.2369609	0.0030774	0.4380653	1370.37	16.04	1455.44	31.88	0.35321486
S22-18_4.6L_g	3.0425626	0.0547875	0.2369222	0.0039343	0.3043970	1369.86	20.44	1489.70	43.09	0.788342936
S22-18_4.7L_e	2.9351244	0.0573402	0.2353408	0.0033981	0.4372310	1361.83	17.73	1424.48	34.77	0.322539471
S22-18_4.7L_g	2.9590617	0.0579569	0.2400914	0.0036147	0.3672303	1386.49	18.74	1407.23	35.28	0.373223262
S22-18_4.7L_k	3.1028461	0.0526792	0.2428324	0.0035991	0.1066285	1400.73	18.67	1483.83	40.06	0.613175159
S22-18_4.7L_l	2.9035250	0.0578824	0.2310913	0.0035974	0.2755452	1339.53	18.78	1425.90	39.13	0.481253062
S22-18_4.8L_e	2.9810700	0.0627037	0.2359970	0.0033436	0.3754322	1365.26	17.46	1452.48	40.24	0.307986103
S22-18_4.9L_a	3.0047923	0.0662909	0.2393878	0.0037636	0.3325773	1382.77	19.57	1444.81	38.99	0.10477623
S22-18_4.14L_e	2.8570851	0.0531383	0.2273001	0.0030665	0.4188157	1319.83	16.10	1447.67	35.80	0.259230652
S22-18_4.15L_f	2.8463275	0.0575782	0.2284555	0.0024196	0.0126380	1326.09	12.66	1422.65	45.06	0.473805942
S22-18_4.17L_c	2.9482259	0.0580488	0.2347600	0.0027886	0.2693042	1358.98	14.58	1441.81	39.29	0.281213795
S22-18_4.17L_i	3.0954270	0.0625452	0.2457149	0.0031445	0.3454077	1415.83	16.26	1441.97	37.24	0.174168269
S22-18_4.17L_k	2.9913692	0.0612248	0.2400685	0.0028235	0.0547074	1388.93	15.30	1415.75	43.08	0.406550771
S22-18_4.18L_a	2.8860526	0.0607099	0.2375215	0.0030636	0.3085994	1373.31	15.93	1373.76	39.32	-0.050817671
S22-18_4.19L_a	2.9413744	0.0689070	0.2395833	0.0036595	0.4125732	1383.83	19.00	1389.15	46.43	0.417901867